Statistical Modelling and Forecasting of the Preston New Road Seismicity

Statistical Modelling and Forecasting of the Preston New Road Seismicity

S. Mancini, M.J Werner, B.J Baptie, M. Segou

Keyworth, Nottingham   British Geological Survey   2020

BRITISH GEOLOGICAL SURVEY

The full range of our publications is available from BGS shops at Nottingham, Edinburgh, London and Cardiff (Welsh publications only) see contact details below or shop online at www.geologyshop.com

The London Information Office also maintains a reference collection of BGS publications, including maps, for consultation.

We publish an annual catalogue of our maps and other publications; this catalogue is available online or from any of the BGS shops.

The British Geological Survey carries out the geological survey of Great Britain and Northern Ireland (the latter as an agency service for the government of Northern Ireland), and of the surrounding continental shelf, as well as basic research projects. It also undertakes programmes of technical aid in geology in developing countries.

The British Geological Survey is a component body of UK Research and Innovation.

British Geological Survey offices

Environmental Science Centre, Keyworth, Nottingham NG12 5GG

Tel 0115 936 3100

BGS Central Enquiries Desk

Tel 0115 936 3143
email enquiries@bgs.ac.uk

BGS Sales

Tel 0115 936 3241
email sales@bgs.ac.uk

The Lyell Centre, Research Avenue South, Edinburgh EH14 4AP

Tel 0131 667 1000
email scotsales@bgs.ac.uk

Natural History Museum, Cromwell Road, London SW7 5BD

Tel 020 7589 4090
Tel 020 7942 5344/45   email bgslondon@bgs.ac.uk

Cardiff University, Main Building, Park Place, Cardiff CF10 3AT

Tel 029 2167 4280

Maclean Building, Crowmarsh Gifford, Wallingford OX10 8BB

Tel 01491 838800

Geological Survey of Northern Ireland, Department of Enterprise, Trade & Investment, Dundonald House, Upper Newtownards Road, Ballymiscaw, Belfast, BT4 3SB

Tel 01232 666595
www.bgs.ac.uk/gsni/

Natural Environment Research Council, Polaris House, North Star Avenue, Swindon SN2 1EU

Tel 01793 411500   Fax 01793 411501
www.nerc.ac.uk

UK Research and Innovation, Polaris House, Swindon SN2 1FL

Tel 01793 444000
www.ukri.org

Website www.bgs.ac.uk
Shop online at   www.geologyshop.com

Foreword

This report is the published product of a study by the British Geological Survey (BGS) and Avonbank Geophysics Ltd that was commissioned by the Oil and Gas Authority (OGA) to research the feasibility of statistically forecasting the microseismicity observed during and after unconventional shale gas development in 2018/2019 by Cuadrilla Resources at its Preston New Road site near Blackpool, UK. The present study extends an earlier commissioned report by the same authors (Mancini et al., 2019), in which we used the 2018 data to calibrate a standard statistical forecasting model (the so-called ETAS model) and assessed its predictive skill. This report extends this work by (1) including the 2019 data, (2) testing basic relationships between operational (pumping) parameters and injection-induced seismicity, (3) improving the ETAS model formulation to account for periods of injection-induced seismicity, and (4) cross-validating the new model, developed using 2018 data, on the 2019 data.

Contents

FIGURES

Plain Language Summary

The present authors were commissioned by the Oil and Gas Authority (OGA) to investigate the efficiency of statistically forecasting the microseismicity observed during and after unconventional shale gas development in 2018 and 2019 by Cuadrilla Resources at its Preston New Road site near Blackpool, UK. The scope of the research was limited by the available time and resources, and we focussed on the following: (i) assessing the relationship between the induced seismicity and operational parameters (namely total injected volume and fluid injection rate), (ii) modifying a popular statistical model of clustered tectonic seismicity to account for injection-induced seismicity, (iii) generating and evaluating probabilistic forecasts of the variable seismicity rate and magnitude distributions as simulated by the model, including cross-validation tests in which we calibrated the model with 2018 data and tested it out-of-sample with 2019 data, and (iv) assessing the processes not (yet) well captured by the model. Our findings can be summarised as follows.

As we reported previously (Mancini et al., 2019), the microseismic datasets now available from hydraulic fracturing operations in the PNR-1z and PNR-2 well at Preston New Road in 2018 and 2019, respectively, represent globally unique opportunities for fundamental research into processes leading to induced seismicity. Insights from the analysis and modelling of these data will eventually contribute to improved operations and seismic risk mitigation strategies. Because the downhole moment magnitudes of both PNR wells are known to be affected by several issues, we made pragmatic choices to obtain a more complete and representative catalogue for the analysis. Pending a re-estimation of moment magnitudes and associated errors, our conclusions should be treated as preliminary.

The relationship between operational parameters and the seismic response of the geological medium to hydraulic fracturing is complicated and non-unique. Prior studies mostly concerned with waste-water injection have linked seismic moment release to injected volume. In the case of PNR, the released moment per unit injected volume varies dramatically between the wells and also between neighbouring hydraulic fracturing stages in the same well. We find that neither PNR well violates a popular upper bound for the moment release for a given injected volume (the so-called McGarr relationship), but the observed magnitude distribution is also consistent with a much higher bound thought to apply in the UK's tectonic setting. The relationship between earthquake counts and injected volume is also non-unique and variable, but the variability is smaller than in the case of seismic moment release. We observe no obvious temporal trend of the seismic response with time. Despite the scatter in the relationship between earthquake count and injected volume, we find that increased seismicity rates tend to be associated with greater volumes (although large volumes can also generate little seismic response), while smaller volumes are associated with lower seismic rates.

Motivated by this finding, we modify a model used for forecasting tectonic clustered seismicity, the Epidemic Type Aftershock Sequence (ETAS) model. Specifically, our modification to the standard ETAS formulation involves a background seismicity rate that is proportional to the injection rate and that simulates the external 'forcing rate' due to the pumping of pressurised fluid. We estimate both well-specific and sleeve-specific constants of proportionality between seismicity and injection rate from both wells. Using ETAS parameters previously obtained from PNR-1z, we conduct multiple probabilistic forecast experiments on both PNR-1z and PNR-2 to assess the predictive skill of this modified ETAS model class.

We find that the modified ETAS model provides better earthquake rate forecasts than the standard model. In particular, the modified ETAS model can capture high rates due to injection periods. This is based on the assumption that the background and injection rates are correlated, that the injection rate is known in advance and that either the well-specific average seismic response or the sleeve-specific seismic response is known. These are best-case scenarios for forecasting, but they

enable the estimation of a constant of proportionality between the background earthquake rate and the injection rate using real-time data.

We also conduct an out-of-sample forecast experiment, in which the modified ETAS model is calibrated on PNR-1z, applied and then evaluated using PNR-2 data. While the model does not perform as well as the PNR-2-specific models, as expected, its estimates are substantially more informative than the standard model, even in periods of high rates. This provides evidence that injection-rate driven ETAS models can contribute to useful probabilistic forecasts in future shale gas developments.

1 Introduction

Seismicity induced by fluid injections is a growing concern. Many countries are witnessing an increased development of subsurface geo-energy reservoirs, including unconventional shale gas development, enhanced geothermal energy systems, wastewater injection, or underground storage of liquid carbon (e.g., Ellsworth, 2013; Keranen and Weingarten, 2018). These activities promote seismicity in previously aseismic regions or increase existing seismic rates. In recent years, induced seismicity in the US and South Korea, for example, has led to significant damages, losses and casualties (Ellsworth et al., 2019; Lee et al., 2019).

The earthquake potential due to subsurface fluid injections remains poorly understood (e.g., Keranen and Weingarten, 2018). Some studies, mostly concerned with seismicity induced by wastewater injection, have argued that the maximum magnitude of induced earthquakes is limited by the injected volume (McGarr 2014). Specifically, McGarr (2014) predicted that the maximum seismic moment increases linearly with the injected volume at a rate equal to the shear modulus whereas others, presented clear evidence that this limit does not hold ubiquitously (e.g., Lee et al., 2019), and that maximum magnitudes are consistent with sampling from an unbounded Gutenberg-Richter distribution (Van der Elst et al., 2016). Moreover, a substantial fraction of wastewater injection and hydraulic fracturing wells in the US appear to be aseismic, at least with current detection capabilities, while other wells spawn seismic events (e.g., Walsh and Zoback, 2016). The factors that control the seismic response to fluid injection remain largely unknown although several hypotheses are now under investigation.

Statistical models of seismicity have shown some promise in capturing the range of seismic responses to fluid injections. Hainzl and Ogata (2005) concluded that fluid-driven seismicity could be separated from 'regular' seismicity dominated by earthquake triggering. Elasto-static Coulomb stress changes are widely believed to be a dominant mechanism for earthquake triggering (e.g. Richards-Dinger et al., 2010). Hainzl and Ogata (2005) employed a frequently used short-term clustering model, known as the Epidemic Type Aftershock Sequence (ETAS) model (Ogata, 1988). They introduced temporal variations in the background rate, which is otherwise commonly assumed to be constant and due to slow tectonic loading in the case of natural seismicity. Bachmann et al. (2011) modelled the seismicity induced in Basel, (Switzerland) during and after the stimulation of a geothermal energy reservoir. Amongst the several statistical models they developed, an ETAS model with a background rate proportional to the flow rate at the well performed best. Mena et al. (2013) developed a multi-model forecast of the Basel seismicity using a logic-tree approach, including the modified ETAS model, a simpler clustered seismicity model and the seismogenic index model by Shapiro et al. (2010). Mena et al. (2013) concluded that unacceptable levels of seismicity could have been forecast several days before the onset of felt seismicity with the prescribed injection plans.

Although physics-based models of injection-induced seismicity have also shown promise, they require lots of information about the subsurface (e.g., Gaucher et al., 2015) and their continuous update under real-time conditions is not trivial. Physics-based models often include the effects of fluid flow and the reduction of effective stress, requiring information about the diffusion of pore pressure complicated by non-linear permeability dependencies and unknown hydraulic connections along poorly constrained fractures. These models appear to work better at larger scale when pore pressure diffusion is dominant (e.g., Langenbruch et al., 2018) but appear more difficult to apply in cases of hydraulic fracturing induced seismicity.

In the UK, unconventional shale gas development by Cuadrilla Ltd. induced seismicity during two well treatments at Preston New Road, Lancashire, namely PNR-1z in 2018, and PNR-2 in 2019 (Clarke et al., 2019). The induced microseismicity datasets and operational parameters of injected volume and injection rates offered us unique opportunities to assess the relationship between operational parameters and induced seismicity, develop statistical forecast models and conduct probabilistic forecasting experiments that determine the models' predictive skills.

In our earlier report of the statistical modelling and forecasting of the PNR-1z seismicity, Mancini et al. (2019) concluded the following: (i) the ETAS model parameters estimated from the PNR-1z data present an absence of magnitude-dependence of clustering, possibly due to the intense periods of induced seismicity during phases of injection, (ii) the model fit the seismic rate relatively well, (iii) the forecast model presented mixed performance during our experiment, performing well between injection periods and during the long pause of operations but failing to capture the high seismic rates during injection periods.

In this study, our goal is to develop those probabilistic seismicity forecasting tools that can help in real-time decision making and risk mitigation techniques. To that end, we develop improved ETAS models that can provide useful probabilistic seismicity forecasts. To guide model development, we first retrospectively investigate the relationship between (i) released seismic moment and injected volume, and (ii) seismicity and injection rates. We find that these relationships are complex, nonlinear and non-unique, but that seismicity generally increases with injection rate.

We then modify the standard ETAS model by introducing a background rate proportional to the injection rate, following the approach of Bachmann et al. (2011), but here applied in the context of hydraulic fracturing rather than enhanced geothermal systems. We calibrate the constant of proportionality by examining seismicity rate during the periods of injection. Using this modified model, as well as the standard ETAS model by Mancini et al. (2019) as a benchmark, we next conduct several seismicity forecasting experiments of the PNR-1z and PNR2 seismicity. The forecast evaluation reveals an improvement of the predictive skills of the new modified model class over the standard version.

2 Methods

2.1 MAXIMUM SEISMIC MOMENT RELEASE

McGarr (2014) proposed that the seismic moment released as a result of fluid injection is limited by the injection volume ΔV multiplied by the shear modulus G, namely:

$$M_0 = G \Delta V \qquad (1)$$

Importantly, this relationship establishes an upper limit rather than prescribing an exact relationship. For example, a significant fraction of potential seismic moment may be released aseismically (McGarr and Barbour, 2018).

The validity of the McGarr (2014) relationship has been widely debated. Keranen and Weingarten (2018) argued that counterexamples exist in which the seismic moment release far exceeded the expected value given the injection volume. These include, amongst others, the wastewater-

injection induced Mw5.0 Fairview, Oklahoma, earthquake, as well as several earthquakes in Canada (Atkinson et al., 2016).

A modified version of the McGarr (2014) relationship was proposed by Shapiro et al. (2010) and Halo et al. (2014). In their version, the relationship between the released seismic moment and injected volume is characterised by a constant of proportionality, named the seismogenic index, which reflects the spatially and temporally variable seismic response. The index can be continually calibrated on real-time seismicity and then used to forecast the maximum magnitude over a relatively short forecast horizon. Verdon and Budge (2018) developed such forecasts in the context of hydraulic fracturing induced seismicity in the Horn River Basin in Canada, while Clarke et al. (2019) provided maximum magnitude forecasts during the PNR-1z treatment.

A different view was provided by Van der Elst et al. (2016). They argued that the maximum magnitudes observed in different fluid injection operations were consistent with those expected to occur if magnitudes were sampled randomly from an untruncated Gutenberg-Richter law after allowing for variations in the absolute rate (i.e. the a-value).

In the context of this debate, we wish to assess the McGarr (2014) relationship with the data from the two PNR wells. Because McGarr only specified an upper limit, a violation of the relationship would constitute strong (additional) evidence against the hypothesis. Observations below the limit, on the other hand, can be explained by several mechanisms, including a lack of a maximum moment (Van der Elst et al., 2016), and therefore would not constitute strong evidence to support the hypothesis.

2.2   RELATIONSHIP BETWEEN SEISMICITY RATE AND INJECTION RATE

Apart from the McGarr (2014) relationship between maximum moment release and injected volume, many operational parameters and other factors have been proposed as important controls on induced seismicity, including injection volume, injection rate, wellhead injection pressure, injection depth and injection into proximity of crystalline basement. Weingarten et al. (2015) assessed the role these factors play in the generation of wastewater-injection induced seismicity in the Central US and concluded that high injection rates are the most likely decisive triggering factor.

While evidence appears strong that injection rate is a dominant controlling factor, we require a quantitative relationship to model and forecast seismicity. Bachmann et al. (2011), Mena et al. (2013) and others assumed a linear relationship between injection rate and seismicity with a constant of proportionality independent of time but variable between operations.

Here, we assess the relationship between injection rate and seismicity rate in detail using the PNR events and high-resolution injection rates. We seek to probe the validity of a linear proportionality between the two observables. We investigate (i) the extent to which seismicity is determined uniquely by injection rate, (ii) whether a linear relationship is appropriate, and (iii) the variability of the constant of proportionality between wells and amongst sleeves. While the results below show considerable complexity, non-uniqueness and temporal variability in the relationship between injection rate and seismicity, we find that the simple linear parameterisation captures the first order effects of hydraulic fracturing and can thus be used to force the background rate of the ETAS model for the purpose of improved forecasts relative to a standard ETAS model.

2.3   THE STANDARD ETAS MODEL

The ETAS seismicity corresponds to a point process with a stochastic spatiotemporal branching evolution, where each earthquake triggers its own offspring events, whose numbers depend on the parent's magnitude and follow an Omori law decay in time (Ogata, 1988, 1998). In the ETAS

model, triggered earthquakes can have a larger magnitude than their parent event. The total seismicity rate λ (or "conditional intensity") of the temporal ETAS model is defined as:

$$\lambda(t \mid H_t) = \mu + \sum_{i:t_i<t} g(t - t_i; M_i), \tag{2}$$

where μ is the background rate, usually assumed to be time-independent, H_t is the history ($t_i < t$) of all preceding earthquakes occurring at times t_i. The triggering function is expressed by empirical relations, according to the form of Ogata (1998):

$$g(t; M) = K e^{\alpha(M-M_{cut})} \cdot c^{p-1}(t + c)^{-p}(p - 1), \tag{3}$$

with a normalised temporal distribution as the second term on the right-hand-side, respectively. The parameter K regulates the short-term aftershock productivity by a parent event with magnitude M equal or above a minimum triggering magnitude (M_{cut}); α establishes the efficiency of earthquakes in triggering aftershocks as a function of magnitude. The second term on the right-hand side of equation (3) is the modified Omori law (Utsu, 1961) describing the distribution of triggered earthquakes in time in terms of a power law decay with exponent p and a short-term constant c.

We estimate the ETAS parameters by means of the maximum likelihood estimation (MLE) approach, with which we obtain the set of parameters that, given the observations (i.e. a seismicity catalogue with N events), maximise the following log-likelihood function (Zhuang *et al.,* 2002):

$$log L(\mu, K, c, p, \alpha) = \sum_{i=1}^{N} log \lambda (t_i \mid H_t) - \int_{T_0}^{T_1} \lambda(t) \, dt, \tag{4}$$

where T_0 and T_1 represent the start and end times for fitting. We use the R package PtProc by Harte (2010) to perform the estimation.

The ETAS model considers the combination of triggering effects from background and evolving seismicity during the learning phase and within each forecast time period for the next forecast window. To improve the ETAS model within the same time interval, and before the next model update, we simulate these future events. According to the simulation algorithm (Zhuang and Touati, 2015): (a) the number of future events is Poisson distributed with a mean rate controlled by the productivity law, (b) the occurrence times are sampled from the modified Omori law, (c) magnitudes are drawn from a Gutenberg-Richter distribution with *b*-value truncated at M_{max}. In tectonic seismicity we take M_{max} consistent with historical seismicity and modern regional strain rates (Rong *et al*., 2016). For higher generations of triggered events, the simulation process is repeated until the number of potential parent shocks eventually dies out.

2.4 MODIFIED ETAS MODEL FOR INJECTION INDUCED SEISMICITY

In this study, we modify the ETAS model to couple the background rate to the time-dependent fluid injection rate $I_r(t)$ according to:

$$\lambda(t \mid H_t) = \mu(I_r) + \sum_{i:t_i<t} g(t - t_i; M_i), \tag{5}$$

where the background rate $\mu(I_r)$ is assumed to be linearly related to the injection rate via a constant of proportionality c_f:

$$\mu(I_r) = c_f \, I_r(t). \tag{6}$$

In Section 5, we assess the validity of this linear relationship qualitatively with the observed seismicity and injection rates from the two PNR wells. Below, we calculate and compare the bulk (average) values of c_f across the two wells. We also assess the temporal stability of the constant by calculating the specific values for each injection period.

2.5 STATISTICAL EVALUATION OF FORECAST MODELS

To assess the robustness of any forecast model, it must be evaluated against data – ideally against independent data and prospectively, as conducted by the global Collaboratory for the Study of Earthquake Predictability (CSEP; Michael and Werner, 2018). The CSEP community provides rigorous measures for the evaluation of forecasts (i) to flag discrepancies between data and model forecasts (lack of consistency) and (ii) to measure relative performance between models (model ranking).

These tests assess consistency with observations, but whether forecasts are informative and useful to end-users depends on the specific context of the decision-making process the forecasts are meant to support. Moreover, since each test is formulated to assesses one or more specific features of the forecast, model rankings can differ when different performance evaluation metric are considered. As a result, no single evaluation measure will characterise the utility of a forecast for all stakeholders. Because of the limited scope of the present study, we focus here on a statistical evaluation of consistency. The consistency tests presented in this report assess whether observations fall into the range of model simulations, e.g. whether the observed number of earthquakes per hour is within the 95% range of the model forecast.

A number of statistical tests (Schorlemmer et al., 2007; Marzocchi et al., 2012 and references therein) are implemented within CSEP. Here, we employ the modified N-test (Zechar et al., 2010) to compare the total number of observed vs. forecasted earthquakes over a precise time horizon. The N-test asks the question: is the observed number of earthquakes consistent with the range of model simulations? If the observed number falls into the tails of the modelled distribution, this identifies a potentially significant discrepancy between model and data.

The N-test is a two-sided metrics that uses two scores under the assumption that the tested forecast is correct: δ_1 to assess the probability of observing at least N_{obs} earthquakes given a forecast of N_{fore}, and δ_2 to evaluate the probability of observing at most N_{obs} earthquakes given N_{fore}. To compute these two quantiles, we use a cumulative mass function F that is constructed from the model simulations:

$$\delta_1 = 1 - F\left((N_{obs} - 1) \mid N_{fore}\right), \tag{7}$$

$$\delta_2 = F\left(N_{obs} \mid N_{fore}\right). \tag{8}$$

We then evaluate the N-test by applying a one-sided significance test and we 'reject' the forecast if either $\delta_1(t) < \alpha$ or $\delta_2(t) < \alpha$, where $\alpha = 0.025$ is the effective significance value (Zechar et al., 2010), such that observations that fall outside the 95% range of the model simulations are flagged as indicating a potentially important discrepancy between model and data. Scientific or practical significance of the discrepancy will depend on the context and usage. "Rejected" forecasts may thus still be good enough to be useful.

Below, we display the results of the N-tests visually – rather than as quantiles scores – by showing the 95% model range and the observed number as either within the range (in green to indicate test was passed) or outside the model range (in red to indicate a failed N-test and a potentially important discrepancy).

An additional evaluation metric that we use here is the root mean square (RMS) error. We use the RMS error to track the evolution of the cumulative absolute difference between the observed and expected seismicity rates. This metric does not consider the whole range of ETAS forecasts but solely measures the typical discrepancy between the mean forecast and the observation. The RMS error is defined as:

$$RMS = \sqrt{\frac{\sum_{j=1}^{T}(N_{fore}^{(j)} - N_{obs}^{(j)})^2}{T}}, \tag{9}$$

where T indicates the number of forecast windows indexed by j, $N_{fore}^{(j)}$ is the mean expected number from the ETAS simulations, and $N_{obs}^{(j)}$ is the observed number in the forecast window.

Other metrics that account for the entire model distribution rather than just the mean are possible and should be pursued in the future. For example, probabilistic scores such as the likelihood score will also capture the range or uncertainty of the model forecast, rather than focus solely on the mean.

3 Summary of Operations

The horizontal PNR-2 well runs roughly parallel to the PNR-1z well and is offset by approximately 200 m. Similar to PNR-1z, a sliding-sleeve completion method was used, with up to 45 possible hydraulic fracture stages with a planned maximum injected volume of 765 m^3 in any single stage. Operations started on 15 August 2019, but only seven of these stages were completed as operations were suspended following a magnitude of 2.9 ML earthquake on 26 August at 07:30 UTC, almost 72 hours after a hydraulic fracture stage on 23 August, that was strongly felt locally at distances of up to a few kilometers from the epicenter. For information regarding the PNR-1z operations, we refer the reader to Clarke et al. (2019) and Mancini et al. (2019).

4 Data

4.1 OVERVIEW

Seismicity during operations in the PNR-2 well was recorded by a downhole geophone array in the adjacent PNR-1z well. Geophone and sleeve locations were not available at the time of writing. Our understanding is that the downhole instruments in PNR-1z were different to those used in PNR-2. The PNR-1z array (to measure PNR-2 induced seismicity) consisted of 12 geophones, ten of which were 15 Hz instruments while two were 3 Hz accelerometers.

The geophones recorded continuously from the onset of operations on 15 August 2019, detecting over 55,000 microseismic events. The event catalogue supplied for the project consisted of origin times, locations and magnitudes of the events as determined by a geophysical processing contractor. No information was available on the method used to locate individual events or the location uncertainties. Typical location uncertainties for downhole microseismic data are around 10-20 m in depth and slightly larger uncertainties in horizontal location. Similarly, although the magnitudes are reported as moment magnitudes (Mw), no information was available on how this was determined or the magnitude uncertainty.

To compare against and complement the downhole catalogue, we accessed source parameters recorded by the combined surface network of the BGS and the operator (Baptie and Luckett, 2019). This network detected only larger events with magnitudes reported as local magnitudes (ML).

The operator also provided us the pumping data, including fluid injection rates of high temporal resolution (minute by minute).

4.2 DATA QUALITY AND CATALOGUE PREPARATION

The PNR-2 downhole catalogue suffers from brief but critical data gaps, resulting in a loss of recorded seismic events, including the largest event, a ML2.9 recorded on 26 August 2019, and presumably some of its aftershocks. To address this issue we filled these gaps with available events recorded during these time periods by the surface catalogue. These events constitute only the largest events that occurred during the gaps, with smaller events apparently irretrievably lost during data transfer and storage.

Both downhole catalogues of moment magnitudes are subject to uncertainties and biases. Corrected moment magnitudes in both downhole catalogues and their relation to the surface local magnitudes is the aim of an ongoing study by Baptie et al. (2020). For the purpose of this study, we adopted a pragmatic approach to prepare improved moment magnitude catalogues, as follows.

Mancini et al. (2019) described how the PNR-1z moment magnitudes were corrected at the upper end because of waveform clipping. According to preliminary analyses by Baptie et al. (2020), the PNR-2 downhole moment magnitudes are underestimated by 0.15 magnitude units. We therefore added this correction factor to each moment magnitude estimation. In addition, we converted the surface MLs that we added to fill the data gaps using the conversion relationship developed by QCon for Cuadrilla's hydraulic fracturing plan (Cuadrilla Resources Inc, 2019).

4.3 EXPLORATORY DATA ANALYSIS

To have a first order look at the PNR-2 microseismicity dataset, we analyse the seismicity response due to the hydraulic stimulation during each stage of operations. When we plot the occurrence times of earthquakes above magnitude -1.5, we do not observe a simple seismic response proportional to fluid injection rates. As an example, in Figure 1 we report the injection rate trends for stages 2 and 7 and compare them to the observed seismicity; while in stage 2 the seismicity rate almost immediately ramps up following the sudden increase in injection rate (Figure 1a-b), in

stage 7 we observe a few minutes delay in the onset of increased seismicity (Figure 1d-e). The selected examples also show that during short, unsteady injection episodes, the seismicity rate remains mostly unchanged. Such variable behaviour, with delays and rate changes, suggests a complex physical mechanism for induced earthquake nucleation where the enhanced injection rate, although being evidently important, is not the only controlling factor.

To further assess the character of seismicity patterns and temporal clustering during injection periods, we use the inter-event times as a useful diagnostic tool (e.g. Hainzl et al., 2006, Touati et al. 2009). Inter-event times simply indicate the time between two successive events and, depending on their distribution within the period of interest, can provide insight into the seismicity patterns and the underlying generating mechanisms. For example, inter-event times between random and independent (Poissonian) occurrence times follow an exponential distribution. Meanwhile, temporal aftershock clustering according to the Omori law will generate power-law distributed inter-event times with a power-law exponent close to the Omori p-value (e.g. Hainzl et al., 2006). The inter-event times in ETAS model simulations follow a combination of these two in a distribution consisting of three parts: (i) extremely short inter-event times up to a few hours are equally likely (a short-term high plateau corresponding to the Omori law up to the constant c-value), (ii) a mid-term power-law decay due to Omori's power law that identifies temporal clustering, and (iii) a long-term exponential decay that lacks clustering and identifies the independent background rate of spontaneous, unclustered earthquakes.

We find that all inter-event time distributions within injection periods at PNR-2 present a good fit with an exponential decay. In particular, Figures 1c and 1f show that we obtain an adequate fit regardless of the presence of a delay in the observed seismic response. This result suggests that, although we cannot exclude a small portion of clustered seismicity masked by the large quantity of externally forced earthquakes, events in these periods are predominantly generated by direct stimulation rather than event-to-event triggering.

These observations (of non-steady rates but approximately exponential inter-event times) also holds for the other stages. We conclude that, a Poisson process of constant rate may capture the gross features of the observed seismicity as a first order approximation. This provides some confidence that modifying the ETAS model to include a (Poissonian) background driven by the injection rate would improve the model over its standard formulation.
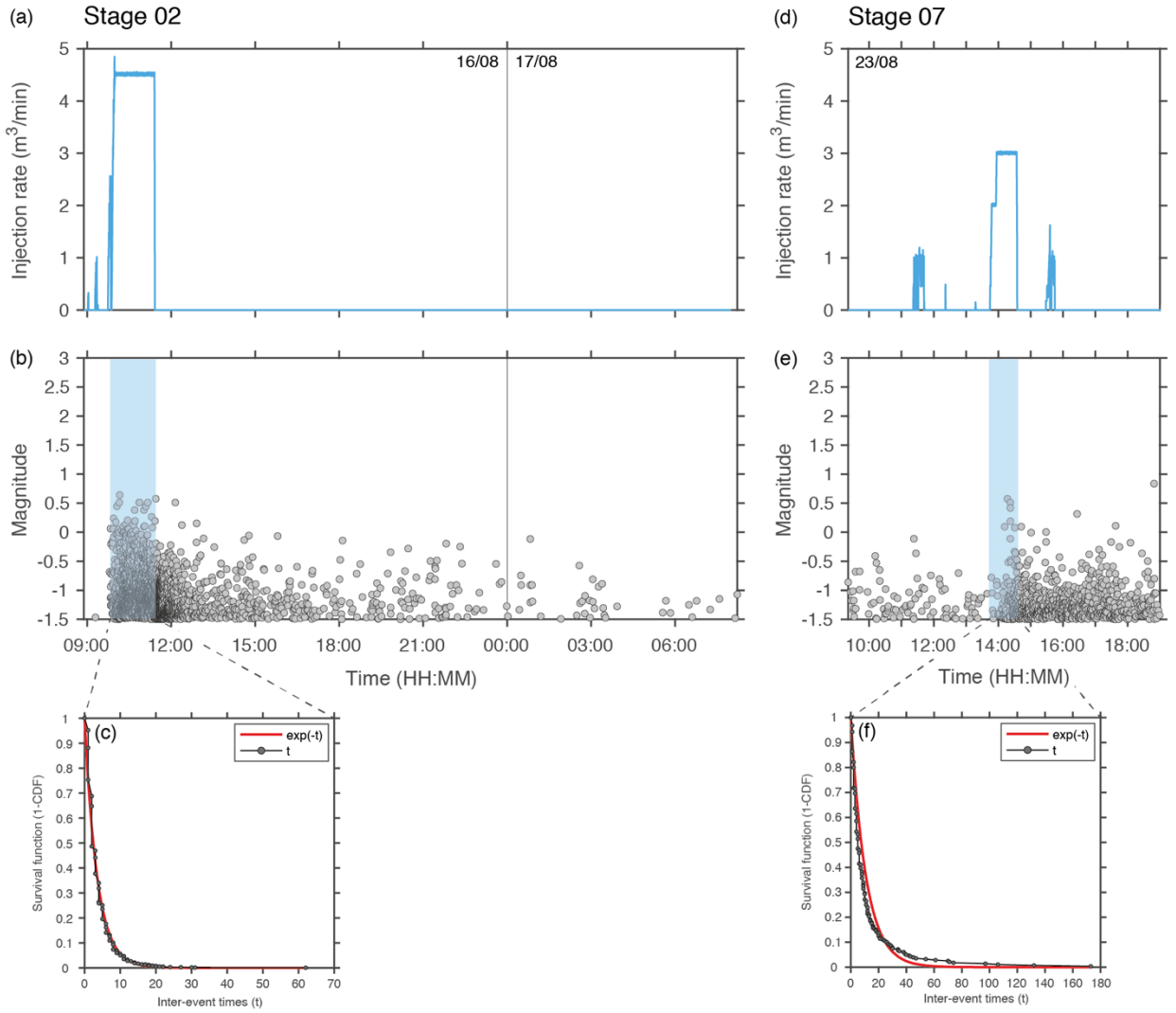
Figure 1. Relationship between injection rates and observed seismicity patters at PNR-2. Panels (a-b) and (d-e) illustrate the seismic rate change in response to heightened injection rates for stages 2 and 7, respectively. Bottom panels (c) and (f) show the inter-event times distribution during the injection periods for the two selected stages.

5 Probing the Relationship between Injection Parameters and Induced Seismicity

5.1 SEISMIC MOMENT RELEASE VERSUS INJECTED VOLUME

To assess McGarr's (2014) upper bound on released seismic moment as a function of total injected volume, and to place the seismic response at PNR into global context, we calculated the cumulative seismic moment (using Mw values and the relationship proposed by Kanamori and Brodski, 2004) and total injected volume for operations in each well. Figure 22 shows that neither well violates McGarr's (2014) upper limit. We do not, however, interpret this as strong support for the hypothesis: Mancini et al. (2019) showed that the PNR-1z magnitude distribution was also consistent with finite sampling from a Gutenberg-Richter law with a conservative tectonic maximum magnitude of 6.5, consistent with the view by Van der Elst et al. (2016). Nonetheless, Figure 22 places the two PNR wells into global perspective.

The two PNR data points on Figure 22 also show dramatic variability in the seismic response despite approximately similar injection volumes into two wells less than a few hundred meters apart and into the same geological unit. Interestingly, despite less injection into PNR-2, more seismic moment was released. This variability suggests that the seismic response in these units and the surrounding crust is at least partially determined by local heterogeneities in the pre-existing stress field.

Figure 2: Seismic moment release against injected volume of the PNR-1z and PNR-2 wells in relation to other fluid injection operations and induced seismicity. Straight line shows the McGarr (2014) relationship for the maximum seismic moment release for a given injected volume. While PNR data do not violate the McGarr relation, they provide only weak support for th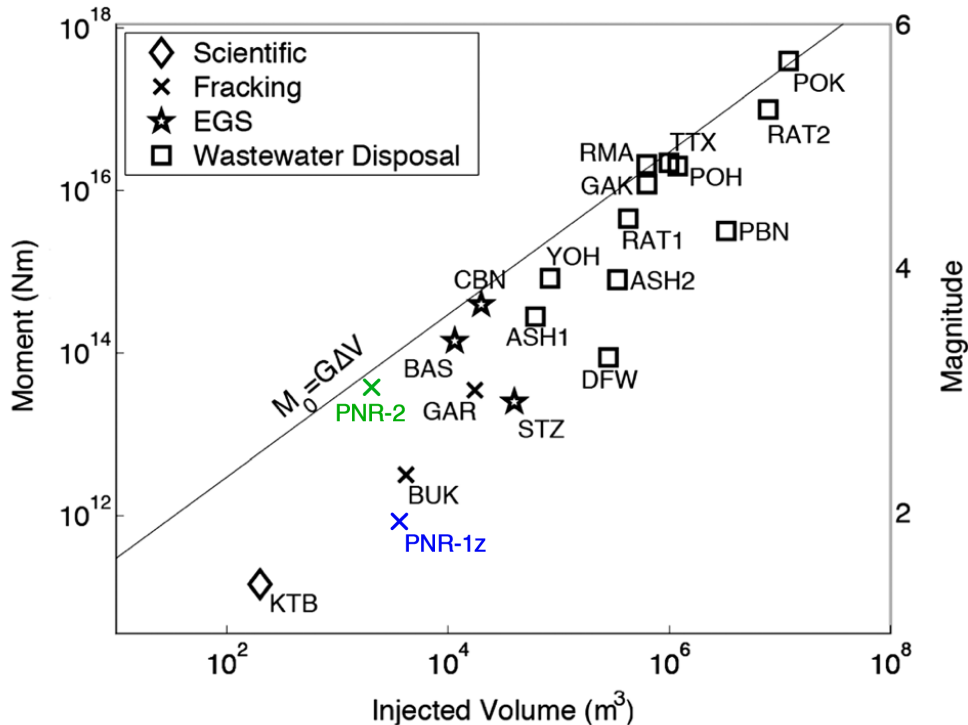e limit. The variability of moment release for similar volumes suggests local stress field heterogeneities at least partially control the moment release.

Figure 33 shows a more granular view of the seismic moment released during each period of injection, revealing a number of interesting first order observations. First, none of the injections generated seismic moments that exceeded the McGarr (2014) relation. Second, the relation between injected volume and released seismic moment is complicated and non-unique. For example, a similar injection volume during injection periods #37b and #32 of PNR-1z generated seismic moments that differ by more than an order of magnitude. Third, later injections do not obviously generate more moment than earlier sleeves. For example, injections #1 and #37b of PNR-1z represent the first and one of the last sleeves, and they receive comparable injection volumes, and yet the later injection #37b generates less seismic moment. The large scatter reveals a complex and non-unique relation between injected volume and released seismic moment, even at the very small scale of neighbouring sleeves.

Despite the large scatter, Figure 33 provides some evidence that moment release increases with injected volume. The least squares linear regressions (in log-space) that we fit to the PNR-1z and PNR-2 data both show positive slopes. Neither regression fits the scattered data particularly well, but they do indicate an overall positive co-dependency. The difference in slopes is surprising for such a small geographical volume of essentially identical geological nature, unless moment release is largely controlled by small scale heterogeneities in the conditions that promote seismic failure.
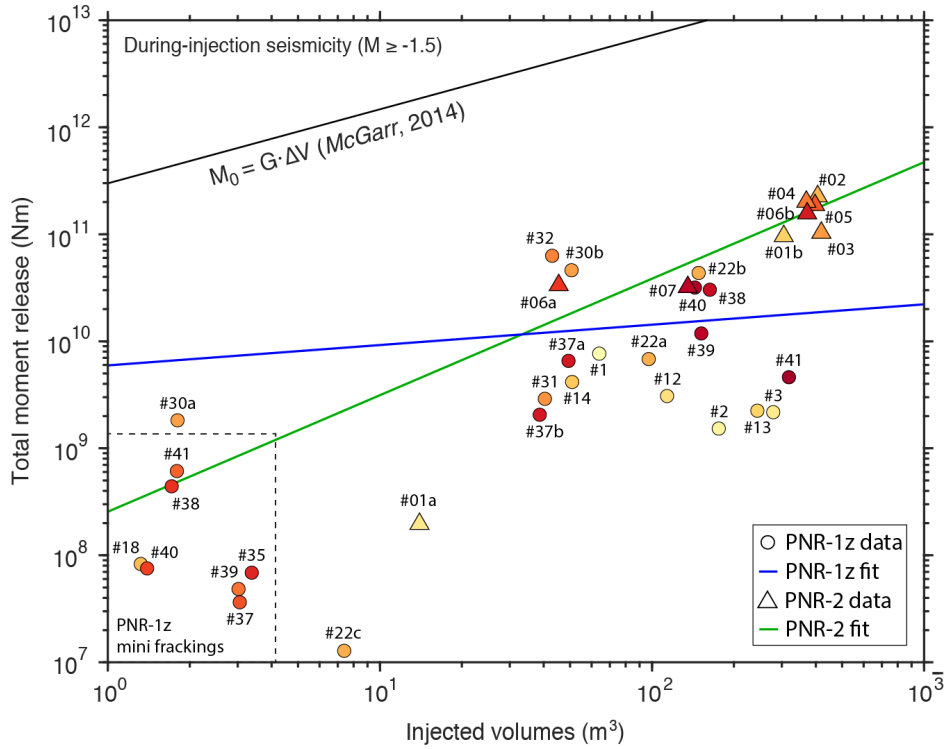
Figure 3: Seismic moment (Mw≥-1.5) released during individual sleeve-specific injection periods against the sleeve-specific injected volumes during PNR-1z (circles) and PNR-2 (triangles). Colours range from yellow to red for increasing sleeve number and time since the start of operations. A number of mini-fracs of the PNR-1z well plot towards the bottom left.

To further illustrate the variability of the relationship between moment and volume, we normalise the released seismic moment by the injected volume during each injection period (Figure 4: Variability of released moment per unit injected volume during (a) PNR-1z and (b) PNR-2. 4). The normalised moment release is essentially the sleeve-wise seismogenic index of the Hallo et al. (2014) model. PNR-1z displays sleeve-to-sleeve variations over three orders of magnitude and shows no increase of seismic susceptibility with increasing sleeve number, *i.e.* time. This implies a substantial a-priori uncertainty of the seismogenic index for any given sleeve. Nonetheless, the sleeve-to-sleeve variability quantified here could be used to make probabilistic estimates of the maximum moment release accounting for uncertainty in the seismogenic index. The resulting uncertainty in the maximum magnitude prediction would correspond to about 2 units of moment magnitude.

Interestingly, PNR-2 displays a relatively stable moment release per unit of injected volume. Except for the period #1a, which corresponds to a mini-frac, the seismic susceptibility varies by about a factor of five. The normalised seismic moments of PNR-2 are also roughly within the range of normalised moments seen during PNR-1z, albeit at the upper end.

In summary, while the seismic response varies dramatically between sleeves and wells within such a small spatial volume, the range of variation appears to also be limited within 10^5 to 10^9 Nm/m^3, at least as observed so far. This is consistent with a non-unique and complex, but broadly positive co-dependency between injected volume and released seismic moment.
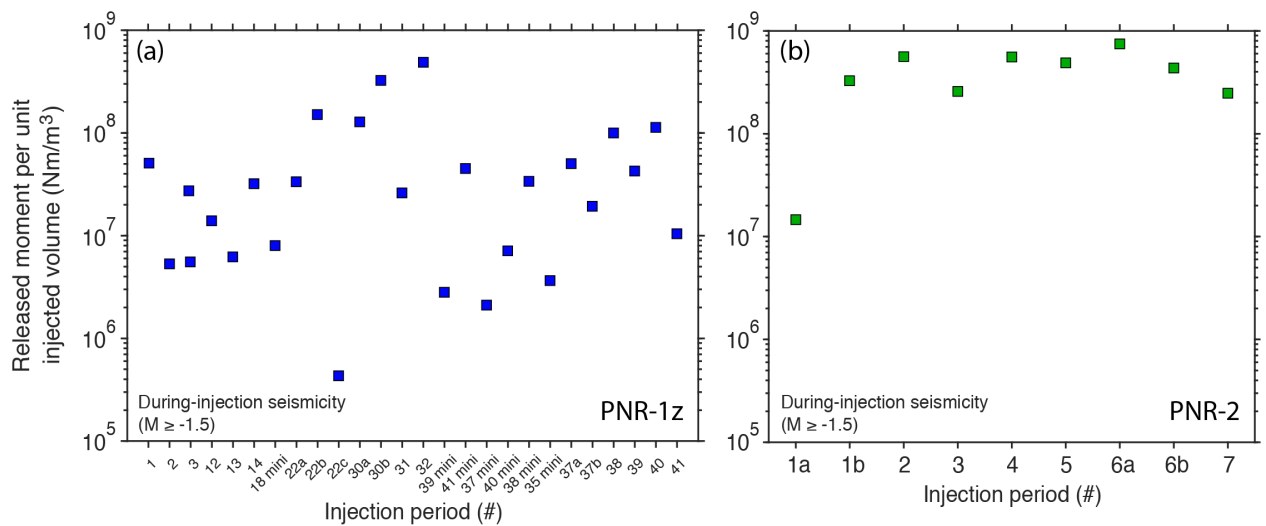
Figure 4: Variability of released moment per unit injected volume during (a) PNR-1z and (b) PNR-2.

5.2 SEISMICITY VERSUS INJECTED VOLUME

Another approach for modelling seismicity induced by fluid injection is to assume that the seismicity grows proportionally with injection volume, i.e. that seismic rate is proportional to injection rate. This places similar but different assumptions on the relationship between the seismic response and anthropogenic forcing than the previously examined hypothesis that seismic moment release is proportional to injected volume. In particular, the relationship is less sensitive to the dominant contribution to the moment by the largest event.

In Figure 5: Seismicity rate (M>-1.5) during injection against injected volume by sleeve for PNR-1z (circles) and PNR-2 (triangles). Colours from yellow to red indicate increasing sleeve number (i.e. increasing time). While the seismicity rate can increase with injected volume, the relationship is complex and non-unique. 5, we show the number of seismic events greater than moment magnitude -1.5 against the injection volume. As before, the data do not show obvious temporal trends. Instead they show a complex and non-unique relationship. While few earthquakes occur during the small injection volumes during mini-fracs, the number of events does not grow uniformly with greater volumes during main stages. For example, injection period #13 of PNR-1z has one of the greatest injection volumes across all stages but generates as few seismic events as a mini-frac with a tenth of the injection volume. Moreover, despite receiving a similar volume as #13 of PNR-1z, injection period #2 of PNR-2 generated over 1,400 events compared with about 100 for #13 of PNR-1z.

As in the previous section, we illustrate in Figure 6: Variability of the earthquake count per unit injected volume as a function of sleeve for (a) PNR-1z and (b) PNR-2.6 the variability of the induced earthquake count by normalising the number by the injected volume, to obtain the normalised earthquake count per unit injected volume across the sleeves of the two wells. The variability of the seismic response per unit volume between the sleeves and wells is about a factor of 10. In this case, however, the seismic responses of some sleeves of PNR-2 (#1b, 2, 3) are greater than any of the PNR-1z sleeves, suggesting that the full range of variability has not yet been observed.

In the present and preceding sections, we analysed the variability of the seismic response to the fluid injection. Our results show that the relationships between released seismic moment or seismicity on one hand, and injected volume on the other hand, are complicated and non-unique. Clearly additional factors play a role in determining the seismogenic potential than solely the

external forcing, even across two wells within a few hundred meters or across sleeves separated by meters.

Despite this complexity, we also observe (i) evidence that both released moment and seismic counts can increase with injected volume and (ii) the variability of the sleeve- or well-specific seismic response is large but appears bounded. These observations motivate us to modify the standard ETAS model by forcing its background rate with the injection rate, as proposed by Bachmann et al. (2011).
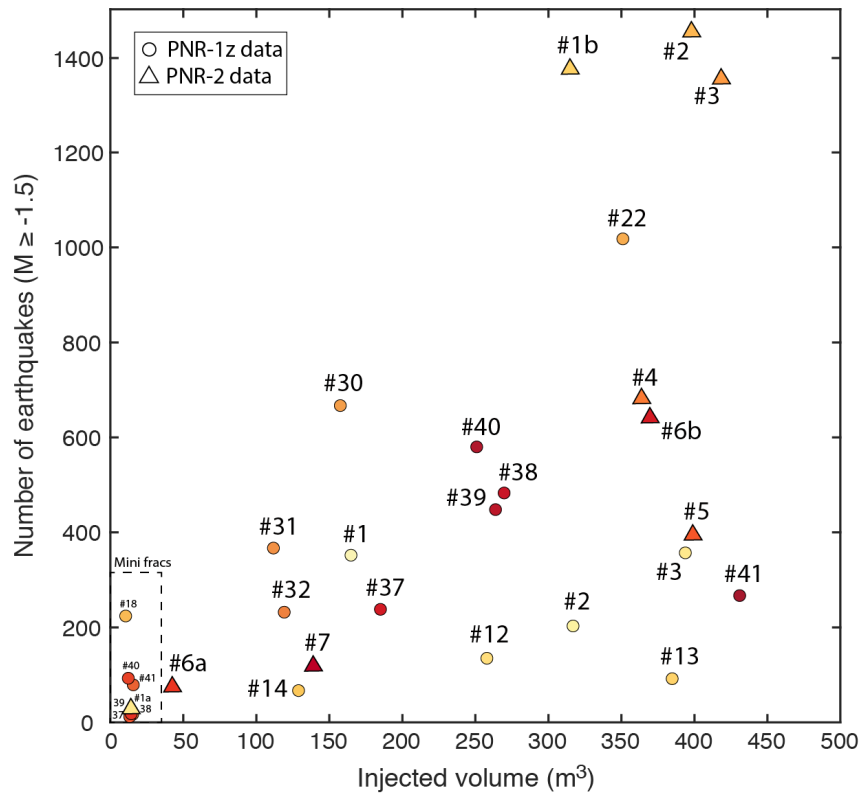

Figure 5: Seismicity rate (M>-1.5) during injection against injected volume by sleeve for PNR-1z (circles) and PNR-2 (triangles). Colours from yellow to red indicate increasing sleeve number (i.e. increasing time). While the seismicity rate can increase with injected volume, the relationship is complex and non-unique.
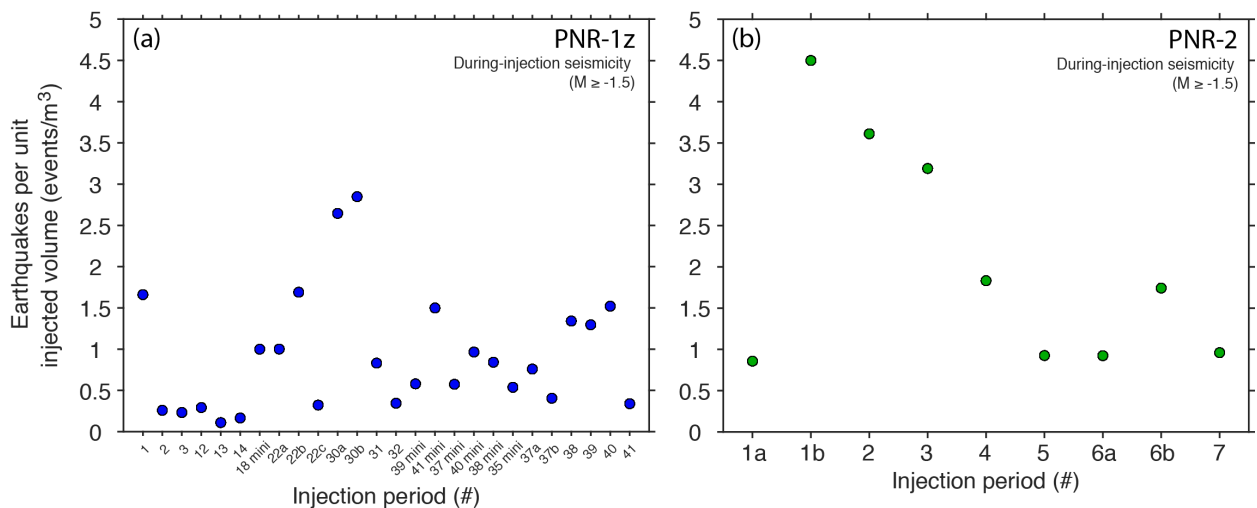

13

Figure 6: Variability of the earthquake count per unit injected volume as a function of sleeve for (a) PNR-1z and (b) PNR-2.

6 Model Calibration and Simulation Framework

6.1 ETAS MODEL CALIBRATION

A detailed analysis and forecast of the magnitude distribution is beyond the scope of this report. However, we briefly summarise here the observations and ETAS model assumptions on the basis of the PNR-1z analysis in our previous report (Mancini et al., 2019).

The ETAS model assumes that magnitudes of simulated seismic events are identically and independently drawn from the exponential Gutenberg-Richter distribution, irrespective of location, history or whether events are spontaneous background or triggered events. The magnitude distribution requires an upper taper or truncation (M_{max}), which we here choose as the most likely regional tectonic maximum of 6.5 (Woessner et al., 2015; Mancini et al., 2019) as well as a b-value. Mancini et al. (2019) estimated a b-value of 1.27 on the basis of the PNR-1z seismicity. Pending finalised moment magnitude estimates of the PNR-2 dataset and an analysis of the b-value, we assume the same b-value for modelling the PNR-2 seismicity. Our conclusions must be viewed as preliminary until the analysis can be repeated with re-estimated, reliable moment magnitudes.

We use the five ETAS parameters (μ, K, α, c, p) that we presented in the previous report (Mancini et al., 2019), obtained by fitting a temporal ETAS model to the PNR-1z microseismicity catalogue by means of maximum likelihood (equation 4). In particular, we implement the set of parameters inverted by considering a catalogue cut-off magnitude of –1.5, and we use this threshold as the minimum triggering magnitude of the ETAS model as well.

Table 1 summarises the ETAS parameters.

Parameter	Value	Description
M_{cut}	-1.5 (fixed)	minimum triggering magnitude
μ	5.367	background rate for standard ETAS
K	0.946	productivity parameter
α	-0.115	productivity scaling parameter
c (days)	0.0020	Omori-Utsu c-value
p	1.757	Omori-Utsu power law decay exponent
b	1.27 (fixed)	Gutenberg-Richter b-value
n	0.91	branching ratio

Table 1. ETAS parameters used for the simulations, taken from the maximum likelihood estimation of PNR-1z seismicity by Mancini et al. (2019)

Mancini et al. (2019) reported that these ETAS parameters are very unusual compared to typical estimates (e.g., Seif et al., 2017). The small productivity exponent α suggests a lack of magnitude-dependent clustering, which we interpret as an artefact due to the model's inability to capture the periods of intense seismicity during injection stages. A re-estimation of the parameters under the modified ETAS formulation was beyond the scope of the present report.

As described in Section 2.4, in the modified ETAS versions we account for an externally driven background rate using the approach of Bachmann et al. (2011), where the background rate is considered proportional to the flow rate. To calculate the constant of proportionality c_f of equation (6), we sample the injection rates and the observed seismicity rates at 1-minute intervals during each injection period at PNR-1z (Figure 7) and PNR-2 (Figure 8). Then, we fit the resulting distribution by imposing a linear fit following the Bachmann et al. (2011) approach and under the assumption that no seismicity is induced when the injection rate is zero. The constant of proportionality is the slope of the fitting line. We perform such linear fit (1) for the entire period of operations to obtain a bulk c_f in each well to be implemented in ETAS-1 models (Figures 7b and 8b) and (2) for individual injection periods to calibrate specific values of the proportionality constant (Figures 7a and 8a show an example from two injection periods at PNR-1z and PNR-2, respectively). As is evident from the scatter plots below, a simple linear relationship between injection rate and observed seismicity rate is an over-simplification of a much more complex pattern; however, a broadly positive co-dependency appears to hold. Results from other stages show similar patterns.

In Figures 7c and 8c we also report two examples of how the expected forced earthquake rate described as a simple modulation of the injection rates compares to the actually observed number of events (grey bars) when (1) c_f values are fitted to the bulk set of injection periods (green lines), (2) c_f values are fitted to the specific injection period data (red lines), and (3) when we use the bulk PNR-1z c_f constant to modulate the seismic response at PNR-2 (orange line).
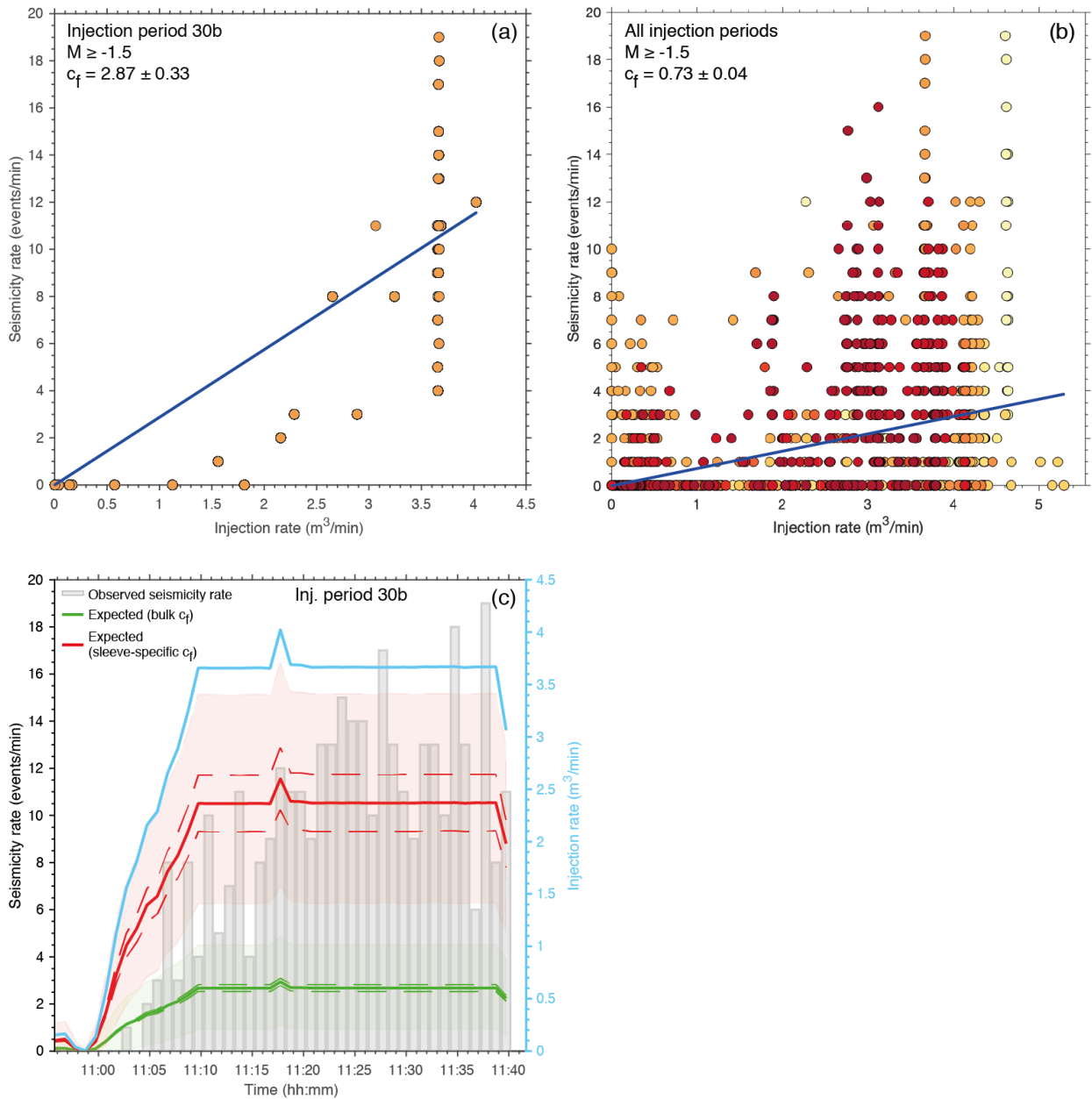
Figure 7: Linear fitting procedure to estimate the proportionality constants c_f between injection rate and seismicity and their effect on the expected rates. (a) sleeve-specific c_f fit for data specific to the injection period 30b at PNR-1z; (b) bulk c_f fit when all PNR-1z injection periods are considered. Colours in (a) and (b) range from yellow to red for increasing time since start of operations. (c) Injection rate driven ETAS background rates at injection period 30b vs. the actually observed seismicity rate sampled at 1-minute intervals (grey bars); shaded areas represent the uncertainty on the expected seismicity rate due to the error on the c_f fitting procedure.
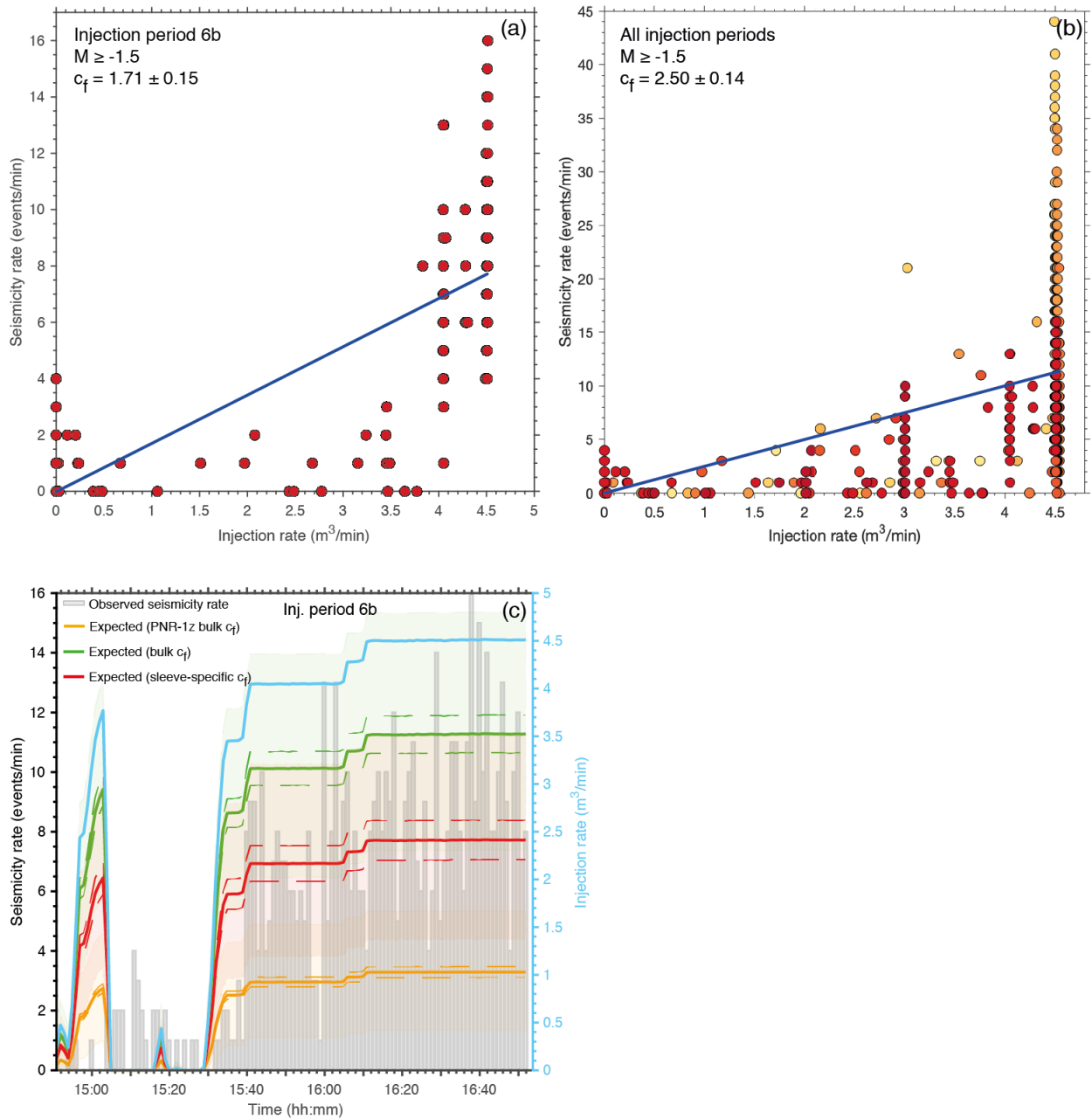
Figure 8: Linear fitting procedure to estimate the c_f constants and their effect on the expected forced rates. (a) sleeve-specific c_f fit for data specific to the injection period 6b at PNR-2; (b) bulk c_f fit when all PNR-2 injection periods are considered. Colours in (a) and (b) range from yellow to red for increasing time since start of operations. (c) Injection rate driven ETAS background rates at injection period 6b vs. the actually observed seismicity rate sampled at 1-minute intervals (grey bars); shaded areas represent the uncertainty on the expected seismicity rate due to the error on the c_f fitting procedure.

17

6.2 FORECASTS BASED ON ETAS SIMULATIONS

All of our ETAS models share some common characteristics, such as: (1) the parameters obtained on the PNR-1z dataset are used to perform 1000 out-of-sample simulations of synthetic catalogues of occurrence times and magnitudes for both PNR-1z and PNR-2 seismicity; (2) ETAS parameters remain fixed during the whole forecast horizon; (3) for both PNR-1z and PNR-2, the start of the simulations corresponds to the start of the operations; (4) simulations are updated hourly or at the beginning of each injection period (whichever comes the sooner). Moreover, each injection period represents a single forecast window, under the assumption that the operator knows in advance the duration and rate of fluid injection.

Mancini et al. (2019) developed a standard ETAS model to forecast the induced seismicity at PNR-1z where the only considered triggering mechanism was the event-to-event interaction (i.e. without explicit consideration of the immediate effect of fluid injection) and showed how such a basic approach resulted in a mixed forecast performance, with some successes during quieter stages and clear failures in periods of high injection rates. We start by testing the same simple forecasting method (ETAS-0) on the PNR-2 seismicity. Subsequently, we modify the standard ETAS formulation as described in Section 2.4. In particular, for both PNR-1z and PNR-2 we test the effectiveness of two modelling strategies:

- ETAS-1 – We sample the injection rate and the seismicity rate at 1-minute windows within all injection periods, then we estimate one average or bulk proportionality constant (c_f) to model the forced seismicity rates occurring at every injection period through equation (6).
- ETAS-2 – We apply the above procedure individually to each stage to derive specific c_f values for each injection period.

Further to ETAS-1 and ETAS-2, we develop an additional forecast version (ETAS-3) where we use the PNR-1z bulk proportionality constant to model the forced seismicity during injection periods at PNR-2. ETAS-3 thus represents a model that provides forecasts for PNR-2 based on a model calibration on PNR-1z. As the model is evaluated out of sample, its performance provides one perspective into how well the models developed here might perform in new hydraulic fracturing operations.

7 Earthquake Rates Forecasts

In this section, we present the forecasts in the form of a comparison between observed and expected incremental evolution of seismicity. Then, we assess the temporal performance of the forecasts using a simple pass/rejection criterion, where a forecast for a time window is accepted if the number of observed earthquakes falls within the 95% confidence bounds of the simulated seismicity range. Finally, we present a metric to quantify the predictive skills of the proposed models based on root mean square errors between the expected and observed numbers.

7.1 STANDARD ETAS MODEL (ETAS-0)

In Figures 9 and 10 we present an example of ETAS-0 timeseries for a subset of the operation stages at PNR-1z and PNR-2. We selected the representative stages in Figures 9 and 10 to encompass the different model performance obtained (over or underprediction) during stages characterised by different pumping rates and variable seismicity patterns (e.g. stages including at least one injection period, stages including only mini-fracks or an extended period of pause/end of operations).

The panels show the observed number of M ≥ -1.5 events per hour together with the mean and 95% confidence interval of the expected ETAS seismicity range. At the start of operations of both PNR-1z (Figure 9a) and PNR-2 (Figure 10a), ETAS-0 projects the onset of the expected high-rate microseismicity with a 1-hour delay with respect to the observations. This undesired effect is due to the lack of M ≥ -1.5 parent earthquakes prior to the earliest forecast time windows. This basic model implementation, in which external fluid forcing is not yet considered, severely underpredicts the seismicity rates of all the injection periods by 1 to 3 orders of magnitude (e.g. Figure 9a,b; Figure 10a,b). However, the model satisfactorily reproduces the number of induced events during mini fracking stages at PNR-1z (Figure 9c), the time decay of seismicity that occurs after and outside the injection periods (e.g. Figure 9d and Figure 10c), as well as the temporal aftershock clustering following the 26 August 2019 Mw 2.8 earthquake at PNR-2 (Figure 10d). We note that the 95% confidence bounds of the forecast often encompass the critical value of zero events, especially during low-rate periods, meaning that the model predicts at least 2.5% probability of no M ≥ -1.5 earthquake occurrence. Such result reveals the intrinsic stochasticity of the ETAS model and reflects the lack of forecast specificity.
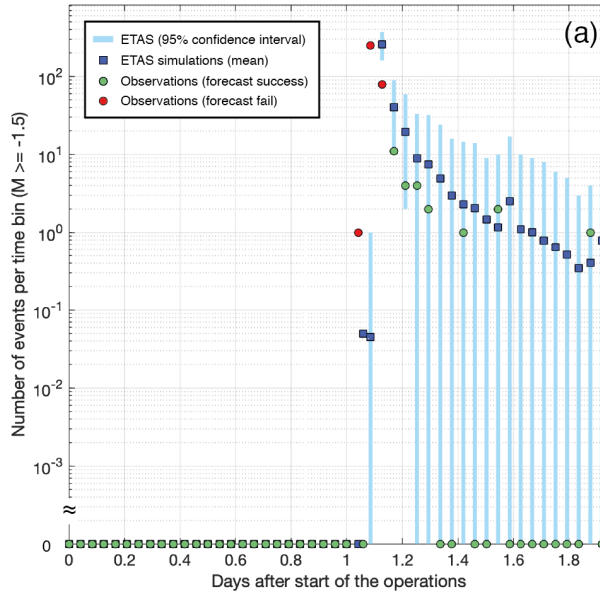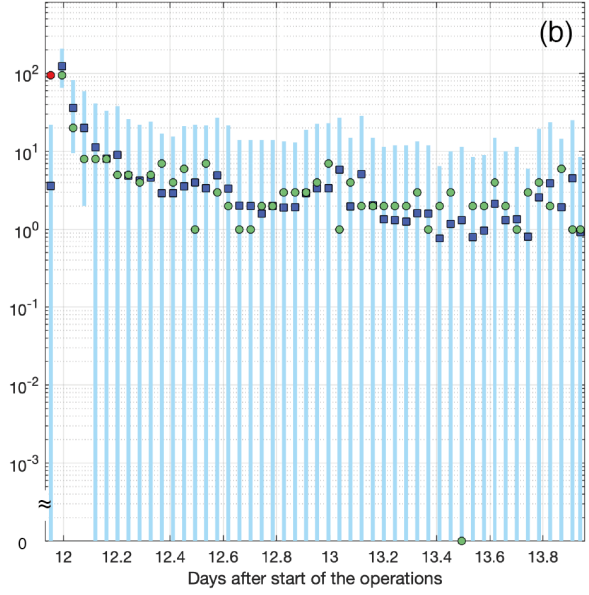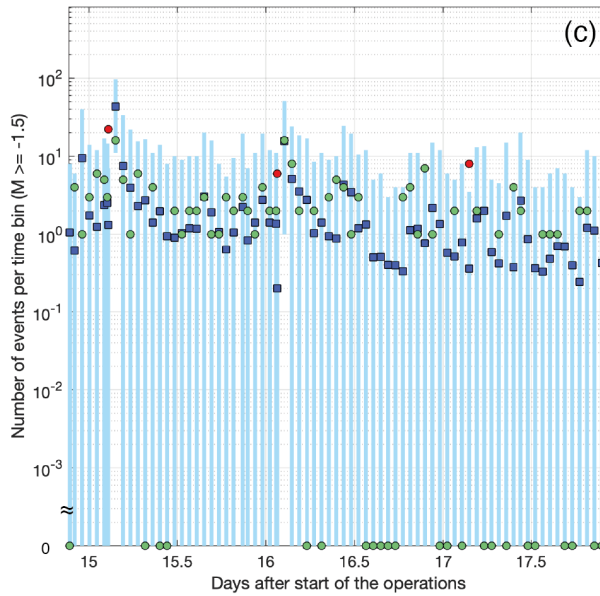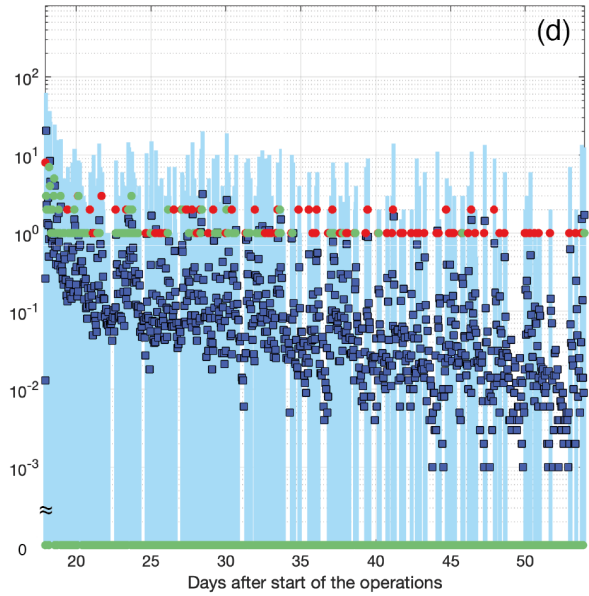
Figure 9: ETAS-0 forecast time series for selected stages at PNR-1z. (a-d) Observed (circles) vs. mean expected (blue squares) hourly number of events. The light blue bars represent the 95% confidence bounds of the ETAS simulations. The colour of the circles indicates whether the observed number of events per hourly time bin falls within (green) or outside (red) the ETAS confidence interval.

Figure 10: Same as Figure 9 but for a subset of selected stages of operations at PNR-2.

7.2 MODIFIED ETAS MODELS

Here, we assess the influence of considering an external forcing rate in the ETAS forecasts as described in Section 2.4 and following the specific modelling assumptions presented in Section 6.3. Hence, from Figure 11 to Figure 15 we extrapolate a selection of stages where at least one injection period occurs, as the implemented ETAS modifications do not exert any effect on the pre/post injection time windows.

Figure 11 and Figure 12 show how ETAS-1 models result in significantly increased expected rates during injection periods, from 2 to 3 orders of magnitudes higher than ETAS-0, providing a remarkably improved visual correlation with the observations. However, their performance related

to those forecast windows characterised by high observed rates (that generally correspond to the fluid injection periods) is highly variable, featuring some successes (e.g. Figure 11c for PNR-1z) and some failures due to both overpredictions (Figure 11b, 12d) and underpredictions (e.g. Figure 11a, 12a-c). Such mixed performance in reproducing the seismicity peaks is likely due to the fact that a single proportionality constant for the whole dataset is not sufficiently representative of the much more complex relationships between injection rate and seismicity rate that are likely to hold at a finer scale (stage-wise or even within each single injection period).

Figure 11: ETAS-1 forecast time series for selected stages at PNR-1z. (a-d) Observed (circles) vs. mean expected (blue squares) hourly number of events. The light blue bars represent the 95% confidence bounds of the ETAS simulations. The colour of the circles indicates whether the observed number of events per hourly time bin falls within (green) or outside (red) the ETAS confidence interval.
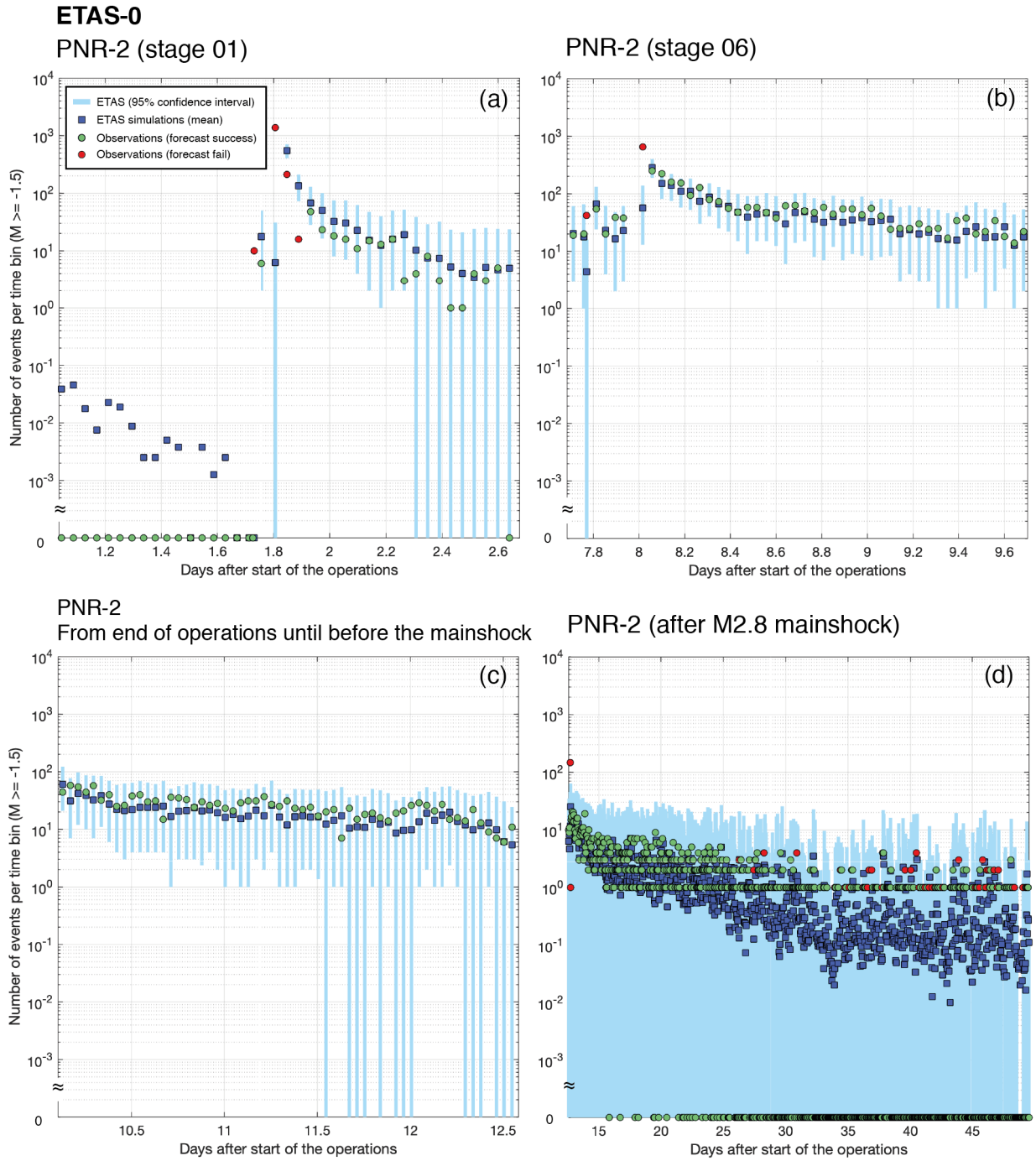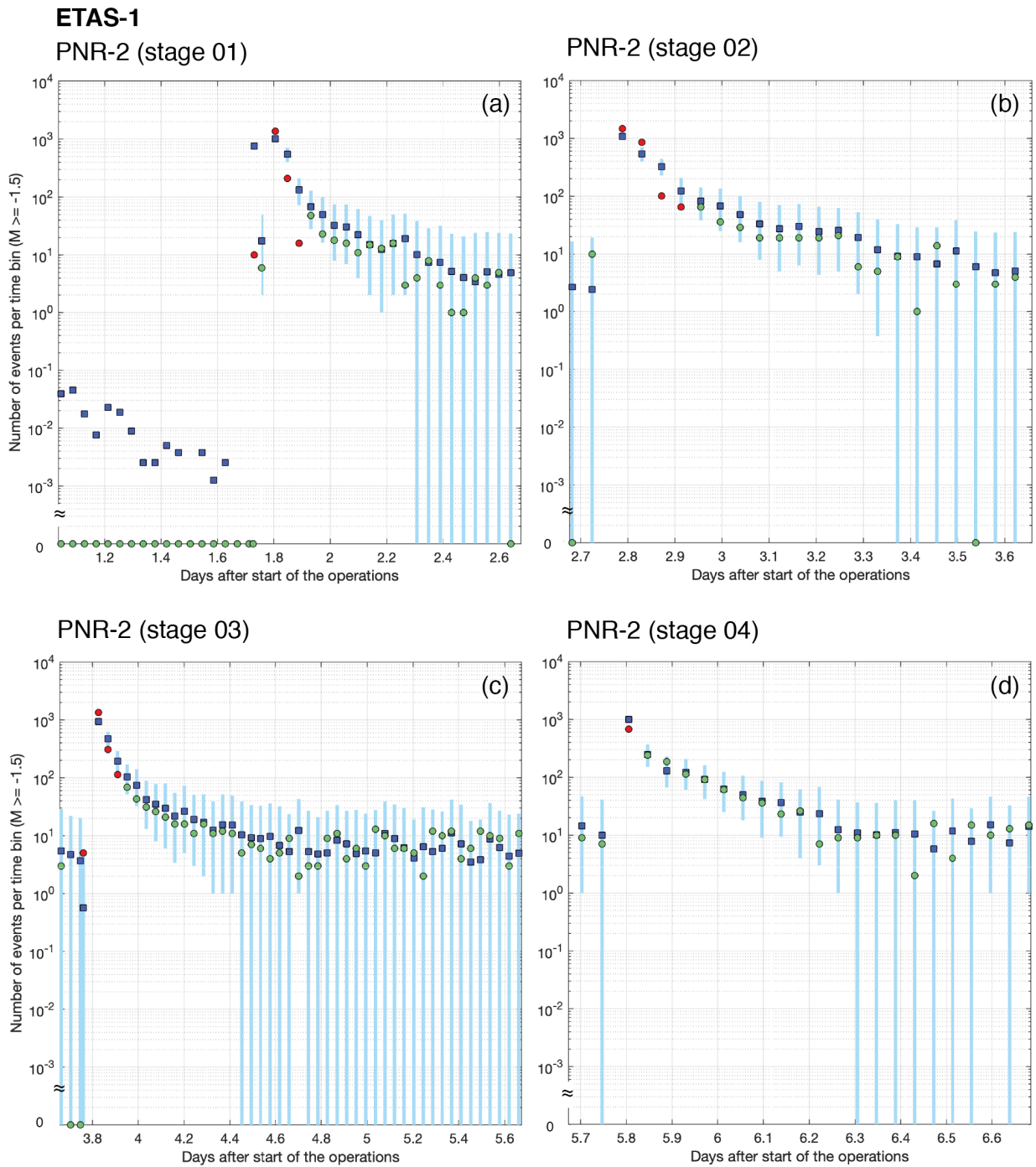
Figure 12: Same as Figure 11 but for a subset of selected stages of operations at PNR-2.

In Figure 13 and Figure 14 we isolate the same stages and show how the forecast changes during the highly active time windows when we use a proportionality constant specific to each injection period. Results show that ETAS-2 mostly compensates for the over/under estimation of the seismicity rates obtained by ETAS-1 during the injection periods. In particular, we observe a much more reliable forecast for high observed rates at PNR-1z (Figure 13 a-c). While the performance improvements related to PNR-1z are notable, those for PNR-2 are mostly limited to the early injection periods (Figure 14a,b) with later stages presenting underestimations of up to 200-300 events that result in model rejections (Figure 14 c,d). This is not surprising, given that the strong variability of the seismicity response even under the same values of injection rate often makes the calibration of a period-specific proportionality constant inaccurate under the simplistic assumption of a linear fit. However, the overall comparison between ETAS-1 and ETAS-2 illustrates how the

effects of such variability are better captured when we parameterise the modified ETAS model using stage-wise pumping data.
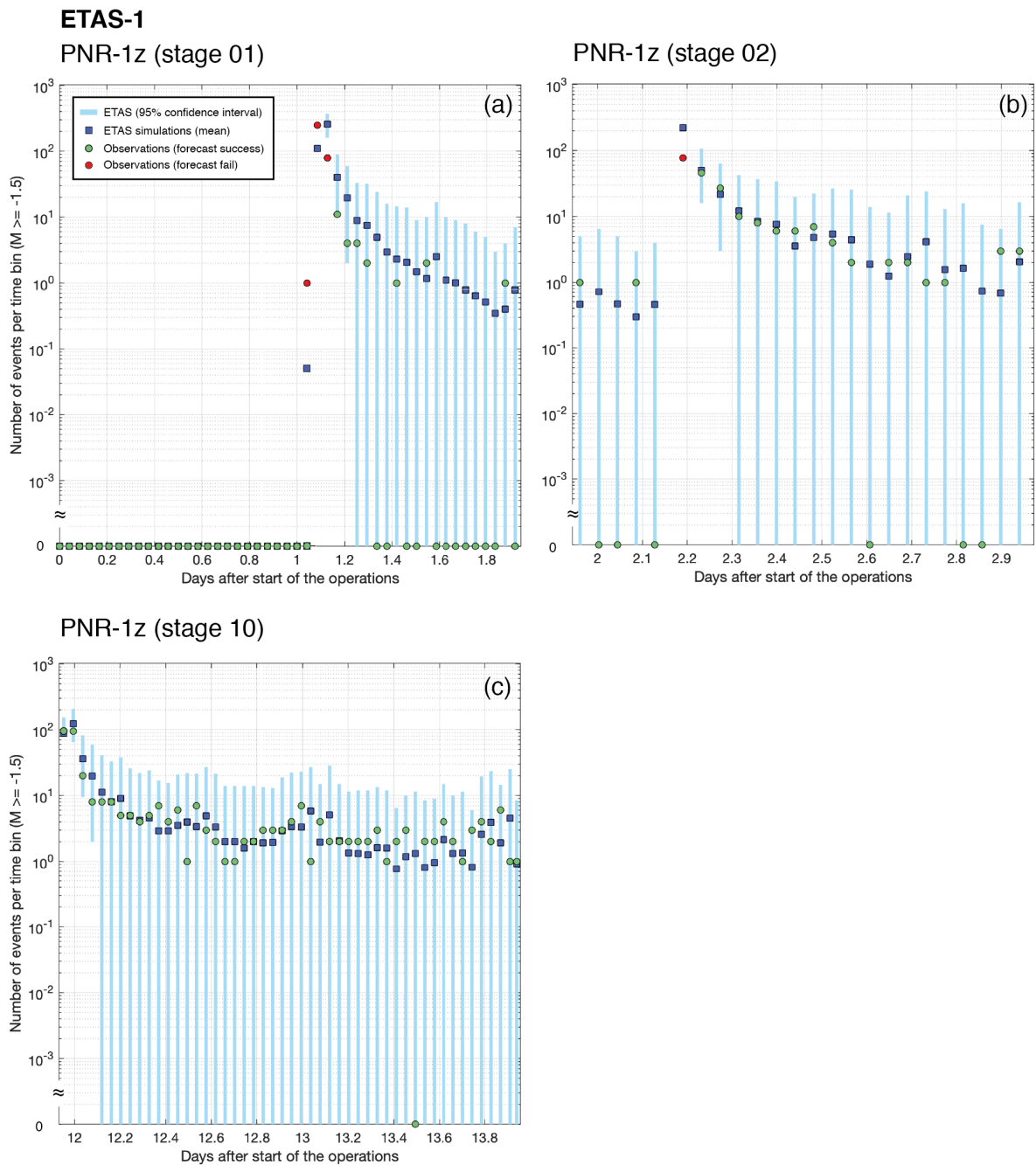

Figure 13: ETAS-2 forecast time series for selected stages at PNR-1z. (a-d) Observed (circles) vs. mean expected (blue squares) hourly number of events. The light blue bars represent the 95% confidence bounds of the ETAS simulations. The colour of the circles indicates whether the observed number of events per hourly time bin falls within (green) or outside (red) the ETAS confidence interval.

ETAS-2
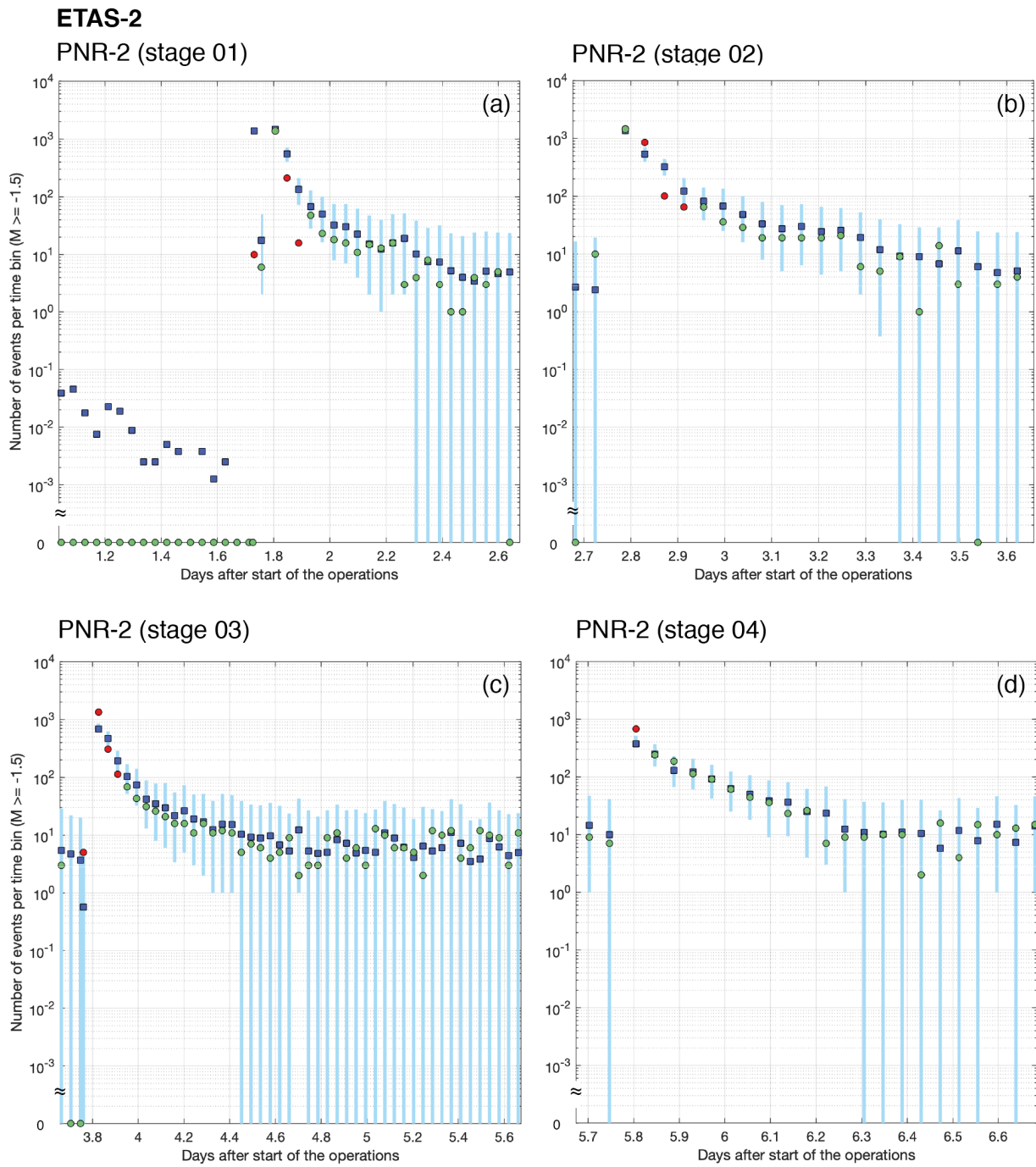
Figure 14: Same as Figure 13 but for a subset of selected stages of operations at PNR-2.

Finally, in ETAS-3 we test the model performance when we use the model calibrated to the PNR-1z data and forecast the injection-induced seismicity at PNR-2. Results show that although ETAS-3 underpredicts rates during many injection periods (Figure 15), it gets much closer to the observations than the standard ETAS-0 model (Figure 10). On one hand, this result indicates the importance of calibrating the modified ETAS model on well-specific pumping data to obtain more reliable results, but it also highlights how crucial it is to include injection data in the ETAS parameterisation applied to HF operations.
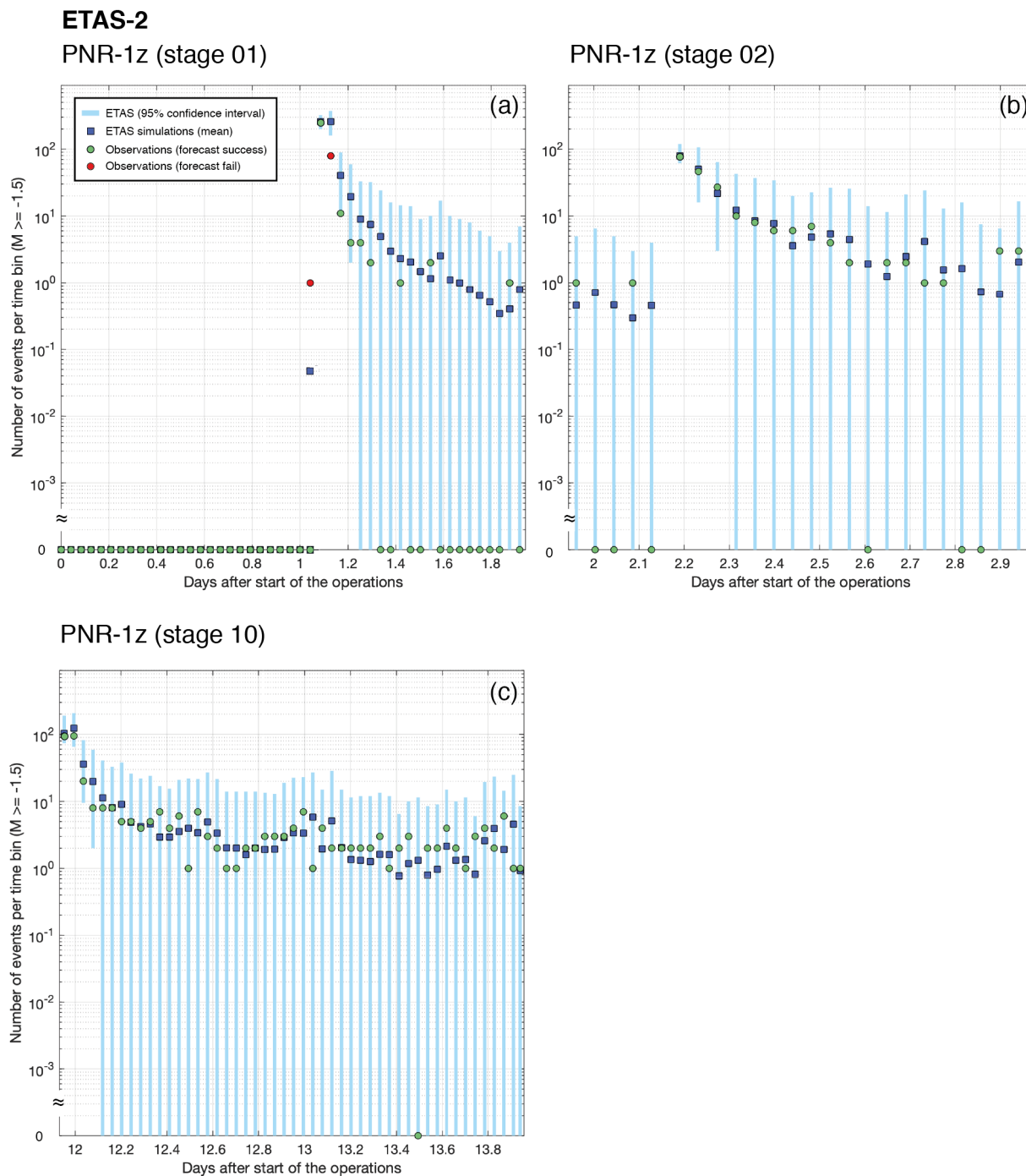

Figure 15: ETAS-3 forecast time series for selected stages at PNR-1z. (a-d) Observed (circles) vs. mean expected (blue squares) hourly number of events. The light blue bars represent the 95% confidence bounds of the ETAS simulations. The colour of the circles indicates whether the observed number of events per hourly time bin falls within (green) or outside (red) the ETAS confidence interval.
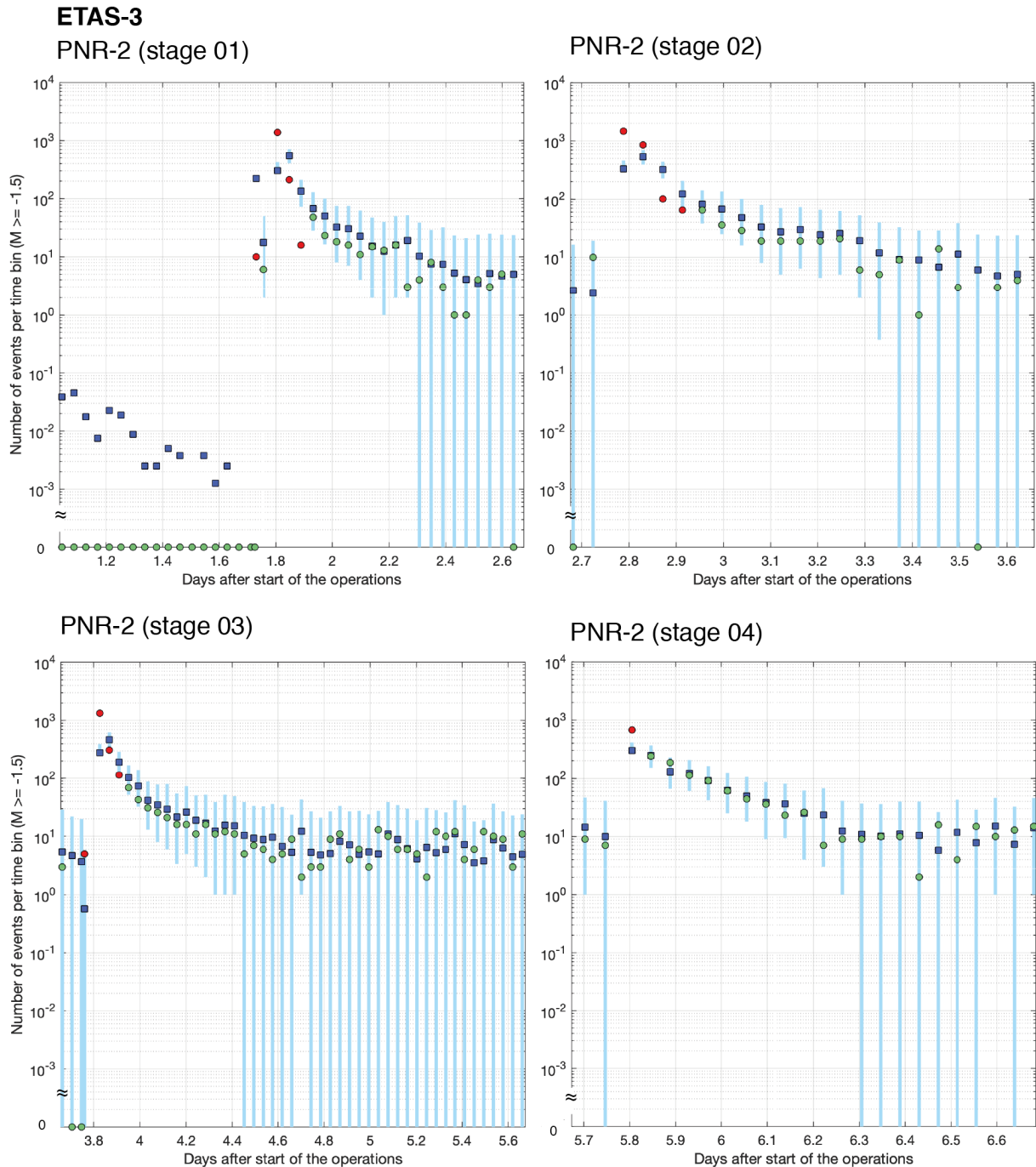
7.3 PERFORMANCE EVALUATION

Here, we compare the capability of the three proposed ETAS models to reproduce the induced events at PNR-1z and PNR-2 during periods of high, moderate or low seismic productivity. For simplicity, we denote a forecast for a specific time window as "accepted" if the observations fall within the 95% confidence bounds of the ETAS simulations, otherwise we mark it as "rejected". More appropriately, "rejected" forecasts highlight a potential discrepancy between data and model, while "accepted" forecasts cannot be rejected.

Figures 16 and 17 show that the vast majority of the forecasts for time windows characterised by low to moderate observed seismicity (i.e. between 0 and 50 M $\geq$ -1.5 earthquakes) cannot be rejected even in the standard ETAS-0 version. Most of these relatively quiet periods represent the activity decay following an injection period where the seismicity appears mostly governed by those event-to-event interactions which are usually well captured by the standard ETAS formulation.

On the other hand, ETAS-0 is frequently surprised by moderate to large numbers of events when it expected very few earthquakes. Such model behaviour results from the lack of coupling between the background rate and the injection parameters; in other words, the model cannot anticipate the enhanced induced seismicity without any information on the external forcing due to fluid injection.

The expected rates during the injection periods increase only when we introduce an additional external forcing in ETAS-1 and ETAS-2. We find that ETAS-2 presents the best predictive skills for moderate (150-250 events) to high (> 350 events) seismicity windows, thanks to the stage-specific model parameterisation. On the other hand, ETAS-1 forecasts, with its bulk proportionality constant between injection rates and seismicity rates, struggle in time windows with more than 200 observed events.

ETAS-2 features a striking performance improvement for PNR-1z (Figure 16c) and is able to reproduce the highest observed seismicity rates at PNR-2 (Figure 17c).
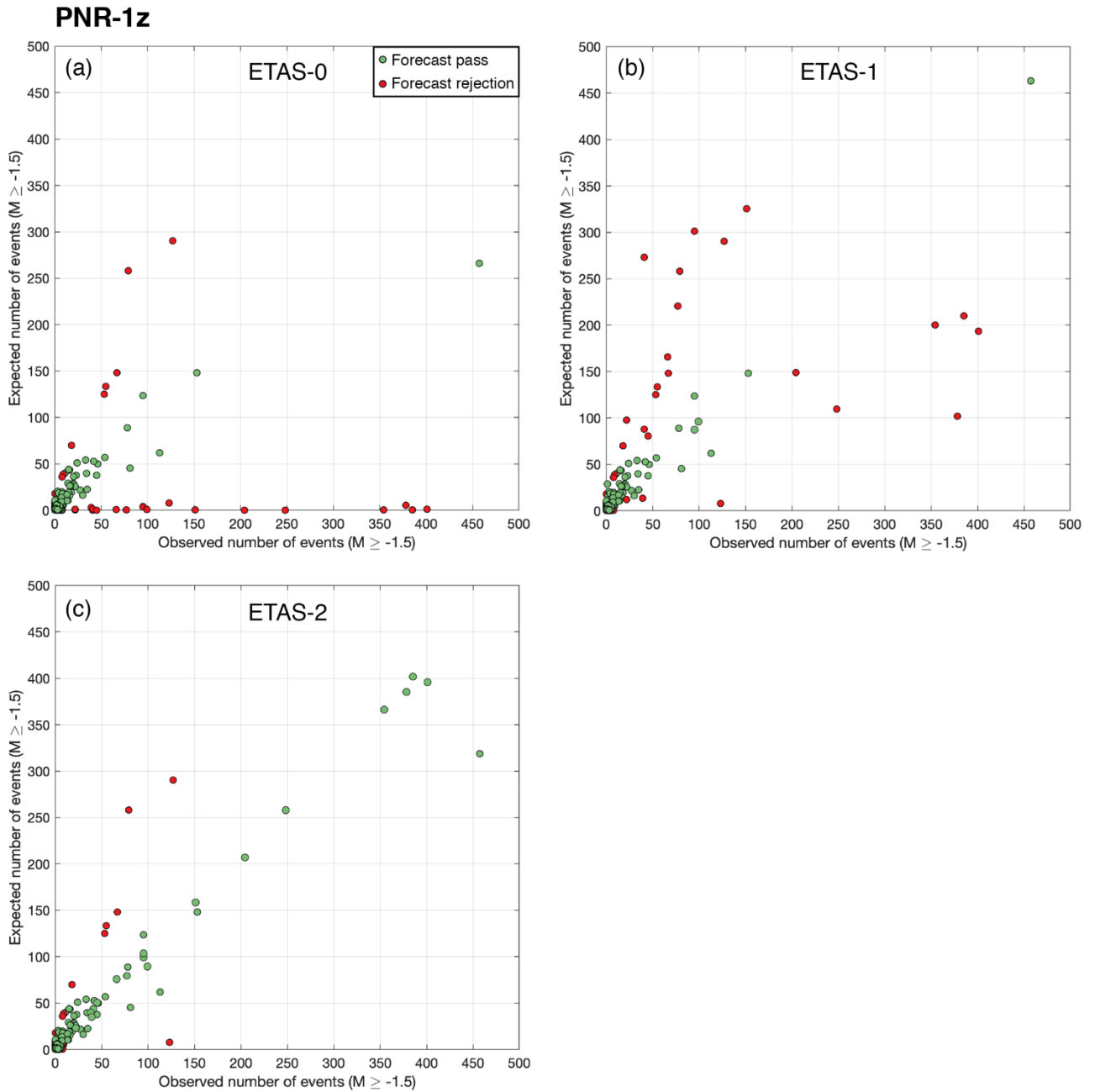
PNR-1z

Figure 16: Observed vs. expected number of events for the three ETAS versions tested on PNR-1z. The red circles indicate forecast rejection, while green ones indicate that the model adequately forecasts the number of events.
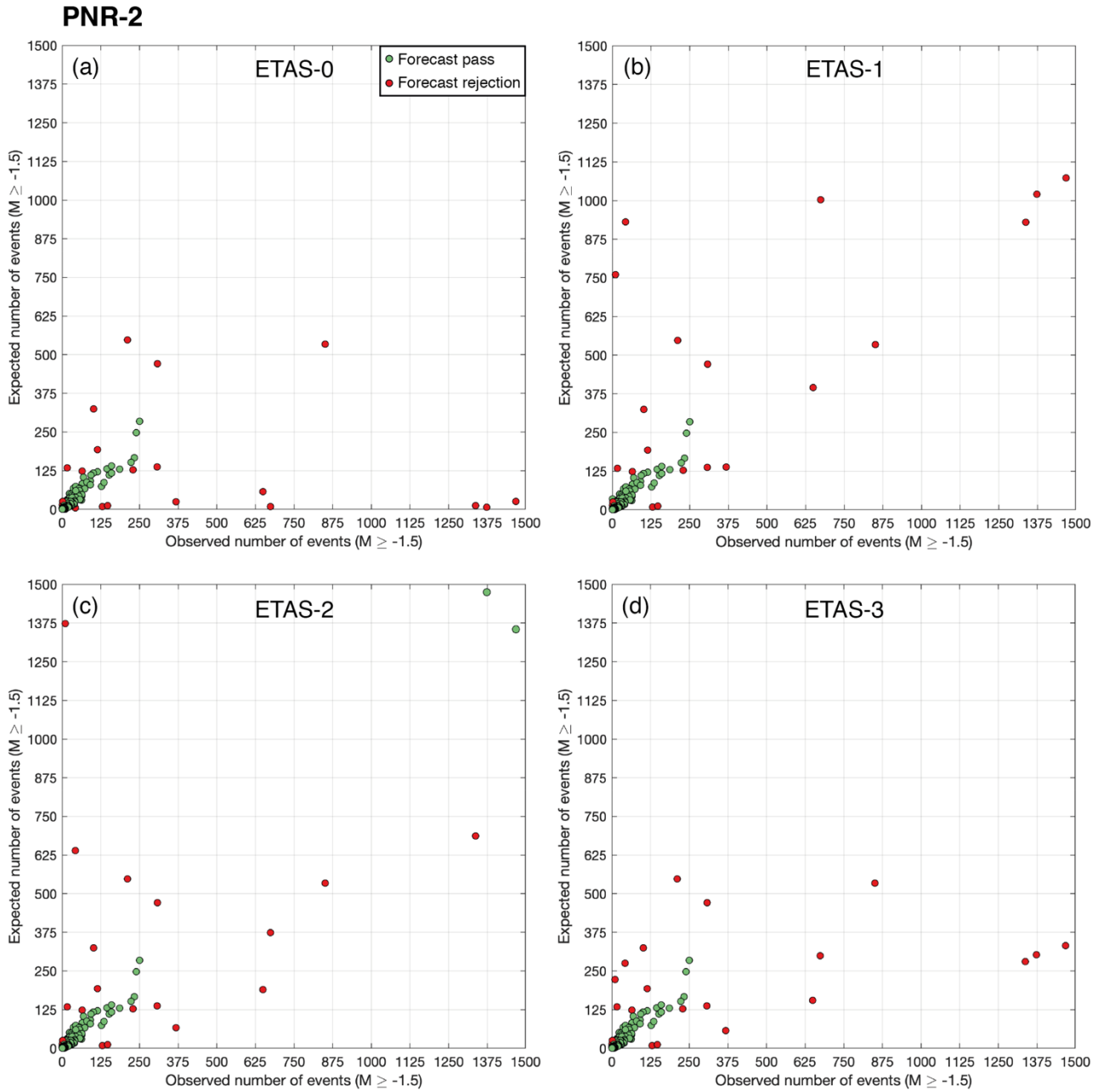
PNR-2

Figure 17: Observed vs. expected number of events for the four ETAS versions tested on PNR-2. The red circles indicate forecast rejection, while green ones indicate that the model adequately forecasts the number of events.

7.3.1 Root mean square (RMS) prediction errors

In Figure 18 we show the RMS error of the proposed models as a function of time. In the case of PNR-1z (Figure 18a), mean ETAS-2 simulations perform best, with RMS errors systematically lower than the other two competing models. ETAS-0 and ETAS-1 show mixed performance within the first 10 days of operations, with ETAS-1 presenting a better overall fit in the medium term, especially when the injection activity resumes following the pause of operations between 3 November – 4 December 2018.

The RMS errors from Figure 18b reveal that also in the case of PNR-2 the ETAS models with the lowest misfit are those modelling the injection-driven rate with a well-specific calibration (ETAS-1 and ETAS-2). However, in this case the RMS errors of ETAS-2 are heavily penalised by the misfit at injection period #1a, making it the second-best performing model after ETAS-1.

The out-of-sample performance of the modified ETAS-3 model is encouraging. Panel b shows that ETAS-3, which uses parameters solely calibrated on PNR-1z data to forecast seismicity at PNR-2, presents better performance than the benchmark ETAS-0 and compares well to the in-sample ETAS-1/2 models. This suggests that an injection-rate-driven ETAS model calibrated on PNR data may perform well in real-time applications during future hydraulic fracturing operations.
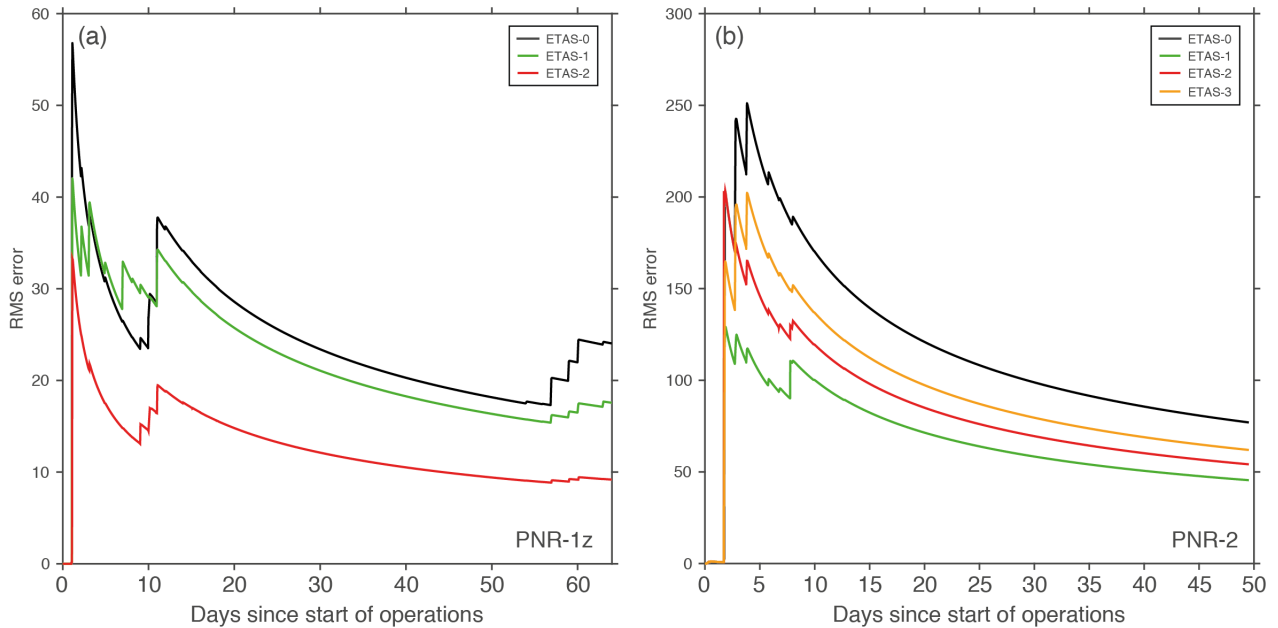

Figure 18: Cumulative root mean square (RMS) errors of the ETAS models as a function of time for (a) PNR-1z and (b) PNR-2.

8 Conclusions

The PNR microseismic datasets present a unique opportunity to develop and evaluate statistical models of hydraulic fracturing induced seismicity. To guide model development, we first assessed two relationships between the operational pumping parameters and the induced seismic events. PNR data do not violate the contentious McGarr (2014) hypothesis that induced seismic moment is limited by injected volume. However, we interpret this result as only weak evidence in support of the hypothesis because other explanations are plausible, including the Van der Elst et al. (2016) argument that maximum magnitudes are as large as statistically expected given low seismic rates and a conservative tectonic maximum magnitude, consistent with model simulations by Mancini et al. (2019) with a tectonic maximum magnitude of Mw6.5.

The relationship between total seismic moment and injected volume is complicated and non-unique, and it appears different between the two wells, despite their close proximity and similar volume injections. We observe no obvious temporal trend (increasing or decreasing) in the seismic moment release or seismic rate with stage number. Between sleeves, the seismic moment released per unit injected volume varied over three orders of magnitude. That is, the same injected volume can lead to seismic moment releases that differ by approximately two moment magnitude units. This variability is a clear indication that the medium's seismic response is at least partially

controlled by locally heterogeneous conditions and physical processes generating seismicity that are not captured by the simple linear relationship. Efforts to predict the moment release and maximum magnitudes using this effective seismogenic index will be adversely affected by this observed variability (in addition to uncertainties in b-values, magnitude scales and magnitude uncertainties).

An analysis of the relationship between the earthquake numbers and injected volume revealed similar findings (a complex and non-unique relationship), but the induced earthquake rate varied less between sleeves than the induced seismic moment.

Notwithstanding the substantial observed variability and thus uncertainty between operational pumping data and induced seismicity, we observe a generally positive co-dependency, which can be exploited to use injection rate to help forecast induced seismicity. This supports an incorporation of operational parameters into the standard ETAS model. On the basis of our analysis of the relationship between seismic rate and injection rate, we modified the ETAS model to include a background rate that is proportional to volume injection rate. The constants of proportionality were assessed in bulk (ETAS-1) and individually for each sleeve (ETAS-2). These models represent best case scenarios because we assume that the injection rate is known exactly in advance and that we know either the sleeve-specific seismic response parameter or the bulk well-specific response parameter. These constants can plausibly be estimated in real-time, although with additional uncertainty.

The modified ETAS models capture the induced seismicity substantially better than the standard ETAS-0 model. In particular, the standard ETAS-0 model occasionally drastically underpredicted the number of events, because its forecasts were not driven by the injection rate. In contrast, the modified ETAS models were much closer in their forecasts of high seismicity rates, although formal tests still show occasional discrepancies.

To mimic an out-of-sample test, we calibrated a modified ETAS model (ETAS-3) on PNR-1z data and evaluated its predictive skill with PNR-2 data. Encouragingly, the model performed comparatively to the in-sample models calibrated on PNR-2 data and outperformed the standard ETAS-0 model. This provides evidence that injection-rate driven ETAS models can contribute to useful probabilistic forecasts in future shale gas developments.

Injection-rate driven ETAS models can also be usefully convolved with ground motion models to create time-dependent probabilistic seismic hazard (and risk) assessments. These probabilistic seismicity and hazard forecasting tools may provide useful information for operators, regulators, residents and other stakeholders. Future model development could focus on (i) capturing better the complex and non-unique relationship between injection rate and seismic response and (ii) real-time parameter estimation for real-time applications.

References

British Geological Survey holds most of the references listed below, and copies may be obtained via the library service subject to copyright legislation (contact libuser@bgs.ac.uk for details). The library catalogue is available at: https://envirolib.apps.nerc.ac.uk/olibcgi.

Bachmann, C., Wiemer, S., Woessner, J., and Hainzl, S. (2011). Statistical analysis of the induced Basel 2006 earthquake sequence: Introducing a probability-based monitoring approach for Enhanced Geothermal Systems, *Geophys. J. Int.*, 186, 793-807.

Baptie, B. and Luckett, R. (2019). Seismicity Induced by Hydraulic Fracturing Operations at Preston New Road, Lancashire, 2018. Proceedings of the Society of Earthquake and Civil Engineering Dynamics Conference, 9-10 September 2019, Greenwich, London.

Baptie, B, Luckett, R, Butcher, A, Werner, MJ, 2020. Robust relationships for magnitude conversion of PNR seismicity catalogues. British Geological Survey Open Report

Clarke, H., Verdon, J. P., Kettlety, T., Baird, A. F., & Kendall, J. M. (2019). Real-Time Imaging, Forecasting, and Management of Human-Induced Seismicity at Preston New Road, Lancashire, England. *Seismol. Res. Lett.*, 90(5), 1902-1915.

Cuadrilla Resources Inc. (2019). Hydraulic Fracture Plan PNR 2. Cuadrilla Resources Inc. Report CORP-HSE-RPT-003.

Ellsworth, W. L. (2013). Injection-induced earthquakes. *Science*, *341*(6142), 1225942.

Ellsworth, W. L., Giardini, D., Townend, J., Ge, S., & Shimamoto, T. (2019). Triggering of the Pohang, Korea, Earthquake (Mw 5.5) by Enhanced Geothermal System Stimulation. *Seismol. Res. Lett.*, 90(5), 1844-1858.

Gaucher, E., Schoenball, M., Heidbach, O., Zang, A., Fokker, P. A., van Wees, J. D., & Kohl, T. (2015). Induced seismicity in geothermal reservoirs: A review of forecasting approaches. *Renew. Sust. Energ. Rev.*, 52, 1473-1490.

Hainzl, S., & Ogata, Y. (2005). Detecting fluid signals in seismicity data through statistical earthquake modeling. *J. Geophys. Res. Solid Earth*, 110(B5).

Hainzl, S., Scherbaum, F., & Beauval, C. (2006). Estimating background activity based on interevent-time distribution, *Bull. Seismol. Soc. Am.*, 96(1), 313-320.

Hallo, M., Oprsal, I., Eisner, L., & Ali, M. Y. (2014). Prediction of magnitude of the largest potentially induced seismic event. *J. Seismol.*, 18(3), 421-431.

Harte, D. (2010). PtProcess: An R package for modelling marked point processes indexed by time, *Rep. Prog. Phys.*, 35(8), 1-32.

Kanamori H. & Brodsky, E.E. (2004). The physics of earthquakes: *Rep. Prog. Phys.* 67, 1429-1496.

Keranen, K. M., & Weingarten, M. (2018). Induced Seismicity. *Annu. Rev. Earth Planet Sci.*, *46*, 149-174.

Langenbruch, C., Weingarten, M., & Zoback, M. D. (2018). Physics-based forecasting of man-made earthquake hazards in Oklahoma and Kansas. *Nat. commun.*, 9(1), 1-10.

Lee, K., Ellsworth, W. L., Giardini, D., Townend, J., Ge, S., Shimamoto, T., Yeo, I., Kang, T., Rhie, J., Sheen, D., Chang, C., Woo, J., and Langenbruch, C. (2019). Managing injection-induced seismic risks, *Science*, 364 (6442), 730–32.

Mancini, S., Segou, M., Werner, M. J., and Baptie, B. J. (2019). Statistical Modelling of the Preston New Road Seismicity: Towards Probabilistic Forecasting Tools. British Geological Survey Commissioned Report, CR/19/068. 39pp.

Marzocchi, W., Murru, M., Lombardi, A. M., Falcone, G., and Console, R. (2012). Daily earthquake forecasts during the May-June 2012 Emilia earthquake sequence (northern Italy). *Ann. Geophys.*, 55(4), 561-567. https://doi.org/10.4401/ag-6161.

McGarr, A. (2014). Maximum magnitude earthquakes induced by fluid injection. *J. Geophys. Res. Solid Earth*, *119*(2), 1008-1019.

McGarr, A., & Barbour, A. J. (2018). Injection-induced moment release can also be aseismic. *Geophys. Res. Lett.*, *45*(11), 5344-5351.

Mena, B., Wiemer, S. and Bachmann, C. (2013). Building robust models to forecast the induced seismicity related to geothermal reservoir enhancement, *Bull. Seismol. Soc. Am.*, 103(1), 383-393.

Michael, A. J. and Werner, M. J. (2018). Preface to the Focus Section on the Collaboratory for the Study of Earthquake Predictability (CSEP): New Results and Future Directions. *Seismol. Res. Lett.*, 89(4), 1226-1228. https://doi.org/10.1785/0220180161.

Ogata, Y. (1988). Statistical models for earthquake occurrences and residual analysis for point processes, *J. Am. Stat. Assoc.*, 83(401), 9–27.

Ogata, Y. (1998). Space-time point-process models for earthquake occurrences, *Ann. Inst. Stat. Math.*, 50(2), 379–402. https://doi.org/10.1023/A:1003403601725.

Richards-Dinger, K., Stein, R. S., & Toda, S. (2010). Decay of aftershock density with distance does not indicate triggering by dynamic stress. *Nature*, 467(7315), 583-586.

Rong, Y., Bird, P. and- Jackson, D. D. (2016). Earthquake potential and magnitude limits inferred from a geodetic strain-rate model for southern Europe. *Geophys. J. Int.*, 205, 509–522. https://doi.org/10.1093/gji/ggw018.

Schorlemmer, D., Gerstenberger, M. C., Wiemer, S., Jackson, D. D., and Rhoades, D. A. (2007). Earthquake likelihood model testing. *Seismol. Res. Lett.*, 78(1), 17–29. https://doi.org/doi:10.1785/gssrl.78.1.17.

Seif, S., Mignan, A., Zechar, J. D., Werner, M. J. and Wiemer, S. (2017). Estimating ETAS: The effects of truncation, missing data, and model assumptions, *J. Geophys. Res. Solid Earth*, 121, 449–469. https://doi.org/10.1002/2016JB012809.

Shapiro, S. A., Dinske, C., Langenbruch, C., & Wenzel, F. (2010). Seismogenic index and magnitude probability of earthquakes induced during reservoir fluid stimulations. *Lead. Edge*, 29(3), 304-309.

Touati, S., Naylor, M. & Main, I. G. (2009). Origin and nonuniversality of the earthquake interevent time distribution. *Phys. Rev. Lett.*, 102(16), 168501.

Townend, J. and Zoback, M.D. (2000). How faulting keeps the crust strong, *Geology*, 28, 5, 399-402.

Utsu, T. (1961). A statistical study on the occurrence of aftershocks. *Geophys. Mag.*, 30, 521-605.

Van der Elst, N J., Page, M.T., Weiser, D.A., Goebel, T.H.W. and Hosseini, S.M. (2016), Induced earthquake magnitudes are as large as (statistically) expected. *J. Geophys. Res. Solid Earth*, 121, 4575– 4590.

Verdon, J. P., & Budge, J. (2018). Examining the capability of statistical models to mitigate induced seismicity during hydraulic fracturing of shale gas reservoirs. *Bull. Seismol. Soc. Am.*, 108(2), 690-701.

Walsh III, F. R., & Zoback, M. D. (2016). Probabilistic assessment of potential fault slip related to injection-induced earthquakes: Application to north-central Oklahoma, USA. *Geology*, 44(12), 991-994.

Weingarten, M., Ge, S., Godt, J. W., Bekins, B. A., & Rubinstein, J. L. (2015). High-rate injection is associated with the increase in US mid-continent seismicity. *Science*, 348(6241), 1336-1340.

Woessner, J, Danciu, L, Giardini, D., Crowley, H, Cotton, F, Grünthal, G, Valensise, G, Arvidsson, R, Basili, R, Betül Demircioglu, M, Hiemer, S, Meletti, C, Musson, Rwm, Rovida, An, Sesetyan, K, Stucchi, and the Seismic Hazard Harmonization in Europe (SHARE) Consortium (2015). The 2013 European Seismic hazard model: key components and results. *Bull. Earth. Eng.*, doi.org/10.1007/s10518-015-9795-1.

Zechar, J. D., Gerstenberger, M. C., and Rhoades, D. A. (2010). Likelihood based tests for evaluating space-rate-magnitude earthquake forecasts. *Bull. Seismol. Soc. Am.*, 100, 1184–1195. https://doi.org/10.1785/0120090192.

Zhuang, J., Ogata, Y., and Vere-Jones, D. (2002). Stochastic declustering of space-time earthquake occurrences. *J. Am. Stat. Assoc.*, 97(458), 369–380. https://doi.org/10.1198/016214502760046925.

Zhuang, J., and Touati, S. (2015). Stochastic simulation of earthquake catalogs, Community Online Resource for Statistical Seismicity Analysis. https://doi.org/10.5078/corssa-43806322.